Published in final edited form as:
*J Mol Biol*. 2008 September 26; 382(1): 56–73. doi:10.1016/j.jmb.2008.06.047.

# Divalent Metal Ion Complexes of S100B in the Absence and Presence of Pentamidine

**Thomas H. Charpentier**[1], **Paul T. Wilder**[1], **Melissa A. Liriano**[1], **Kristen M. Varney**[1], **Edwin Pozharski**[2], **Alexander D. MacKerell Jr**[2], **Andrew Coop**[2], **Eric A. Toth**[1,*], and **David J. Weber**[1,*]

[1]Department of Biochemistry and Molecular Biology, The University of Maryland School of Medicine, 108 North Greene Street, Baltimore, MD 21201, USA

[2]Department of Pharmaceutical Sciences, The University of Maryland School of Pharmacy, 20 Penn Street, Baltimore, MD 21201, USA

## Abstract

As part of an effort to inhibit S100B, structures of pentamidine (Pnt) bound to $Ca^{2+}$-loaded and $Zn^{2+}$,$Ca^{2+}$-loaded S100B were determined by X-ray crystallography at 2.15 Å ($R_{free}$ = 0.266) and 1.85 Å ($R_{free}$ = 0.243) resolution, respectively. These data were compared to X-ray structures solved in the absence of Pnt, including $Ca^{2+}$-loaded S100B and $Zn^{2+}$,$Ca^{2+}$-loaded S100B determined here (1.88 Å; $R_{free}$ = 0.267). In the presence and absence of $Zn^{2+}$, electron density corresponding to two Pnt molecules per S100B subunit was mapped for both drug-bound structures. One Pnt binding site (site 1) was adjacent to a p53 peptide binding site on S100B ($\pm Zn^{2+}$), and the second Pnt molecule was mapped to the dimer interface (site 2; $\pm Zn^{2+}$) and in a pocket near residues that define the $Zn^{2+}$ binding site on S100B. In addition, a conformational change in S100B was observed upon the addition of $Zn^{2+}$ to $Ca^{2+}$–S100B, which changed the conformation and orientation of Pnt bound to sites 1 and 2 of Pnt–$Zn^{2+}$,$Ca^{2+}$–S100B when compared to Pnt–$Ca^{2+}$–S100B. That Pnt can adapt to this $Zn^{2+}$-dependent conformational change was unexpected and provides a new mode for S100B inhibition by this drug. These data will be useful for developing novel inhibitors of both $Ca^{2+}$-and $Ca^{2+}$,$Zn^{2+}$-bound S100B.

### Keywords

S100B; pentamidine; X-ray crystallography; zinc; calcium

## Introduction

There are more than 20 S100 proteins originally named because of their solubility in 100% saturated ammonium sulfate.[1] Like calmodulin and most other EF-hand-containing proteins, S100 proteins typically function as a calcium-activated switch that binds and regulates the biological function of numerous protein targets (Fig. 1).[2-5] A unique feature for several S100 proteins is that they also bind $Zn^{2+}$ ($K_d \sim$ 90 nM; S100B) at a structurally conserved site that



*Corresponding authors. E-mail addresses: etoth001@umaryland.edu;dweber@umaryland.edu.

Accession codes
The coordinates for the $Zn^{2+}$,$Ca^{2+}$–S100B, Pnt–$Ca^{2+}$–S100B, and Pnt–$Zn^{2+}$,$Ca^{2+}$–S100B X-ray structures were deposited in the PDB[80,81] and assigned the following accession numbers: $Zn^{2+}$,$Ca^{2+}$–S100B: 3CR2; Pnt–$Ca^{2+}$–S100B: 3CR4; Pnt–$Zn^{2+}$,$Ca^{2+}$–S100B: 3CR5.

is separate from the EF-hand calcium-binding loops.[6-11] Although the biological function of $Zn^{2+}$ binding is not completely understood, it is not considered a structural ion since S100 proteins are typically stable, folded, and active in its absence. Instead, $Zn^{2+}$ likely plays a regulatory role by modulating the affinity of various S100 proteins for $Ca^{2+}$ and/or protein targets, which has been observed *in vitro* for several S100 proteins, including S100B.[2,5,8,12-15]

Members of the S100 protein family are distributed in a cell-specific manner,[3,4,16] including those in a large number of human cancers.[17-19] For S100B, protein levels are elevated in malignant melanoma,[19] anaplastic astrocytomas,[20,21] and glioblastomas.[22] In the case of malignant melanoma, high concentrations of S100B correlate directly with poor prognosis in patients,[23,24,25] and hence, it is used as a clinical marker for this and other cancers. In more recent mechanistic studies, S100B was found to bind directly to the p53 tumor suppressor protein in primary human malignant melanoma cells, reduce p53 protein levels, and inhibit wild-type p53 functions.[6,26-30] Therefore, elevated levels of S100B contribute to cancer progression by down-regulating wild-type p53 protein.[30] Correspondingly, p53 protein levels and its associated activities were restored in malignant melanoma when S100B expression was inhibited by siRNA (small interfering RNA).[29] With these $siRNA^{S100B}$ results in mind, a rational drug design approach was initiated to develop small-molecule inhibitors that bind $Ca^{2+}$–S100B, prevent S100B–p53 complex formation, and restore p53-dependent tumor suppression in cancers with wild-type p53 such as malignant melanoma.[31-33] Furthermore, engineering inhibitors of the $Ca^{2+}$,$Zn^{2+}$-bound form of S100B may also be important since $Zn^{2+}$ homeostasis is disrupted and its levels are typically elevated in patients with skin cancer.[34-37]

Atomic structures of S100B in the $Ca^{2+}$- and p53 peptide-bound states together with computer-aided drug design and high-throughput screening approaches were used to identify small molecules that bound S100B.[31-33] One such compound, pentamidine (Pnt), was characterized by NMR and found to interact with aromatic residues in helix 4 and the C-terminal loop of $Ca^{2+}$–S100B.[31] To pursue this S100B–drug interaction further, we determined the X-ray crystal structures of Pnt bound to divalent metal ion complexes of S100B in this study. In the calcium-bound state, S100B was found to bind two Pnt molecules per S100B subunit with one molecule located near the p53 peptide binding site (termed site 1), as predicted previously.[31] The second Pnt molecule bound a separate site (site 2) at the dimer interface of $Ca^{2+}$–S100B and near residues of the unoccupied $Zn^{2+}$ site. However, in the presence of $Ca^{2+}$ and $Zn^{2+}$, the conformation and relative orientation of both S100B-bound Pnt molecules were different from that observed in the presence of $Ca^{2+}$ alone. Together, the two S100B–Pnt structures will be important for developing novel, high-affinity inhibitors of $Ca^{2+}$–S100B in the absence and presence of $Zn^{2+}$, which could have clinical benefits for treating cancers with elevated levels of S100B.

## Results

The binding of S100B to p53 down-regulates tumor suppressor activity in cancer cells such as malignant melanoma[29,38]; thus, a search for small molecules that bind S100B and prevent S100B–p53 complex formation was undertaken.[31,33] For one such molecule, Pnt, a model for drug binding was reported based on chemical shift perturbations, saturation transfer difference (STD) data, and several intermolecular nuclear Overhauser enhancement constraints.[31] Here, the structure of this Pnt–$Ca^{2+}$–S100B complex was solved using X-ray crystallography. Due to the relatively high levels of $Zn^{2+}$ found in skin and in skin cancers such as malignant melanoma,[36,37,39] these studies were extended to also include a detailed examination of the interaction between Pnt and $Zn^{2+}$,$Ca^{2+}$–S100B.

### Thermodynamic binding studies

As reported previously,[31] the interaction between Pnt and S100B was confirmed to be calcium dependent [isothermal titration calorimetry (ITC): $^{Pnt}K_d$=53±10 μM; fluorescence: $^{Pnt}K_d$=39 ±3 μM; Fig. 2]. However, additional experiments showed that two Pnt molecules bound each S100B subunit with indistinguishable affinities but weaker than that reported previously for the F43W mutant of S100B ($K_d$~1 μM)[31] (Table 2; Fig. 2a). Under the same conditions, Pnt was also found to bind $Zn^{2+}$,$Ca^{2+}$–S100B by ITC ($^{Pnt}K_d$=64±15 μM; Table 2); however, when the Pnt:S100B subunit ratio approached 2:1 in these titrations, some precipitation was observed. To avoid precipitation, we also monitored the binding by titrating both $Zn^{2+}$ and S100B (at a 1:1 ratio) into a solution of Pnt and monitoring the change in Pnt fluorescence ($^{Pnt}K_d$ =39±5 μM; Table 2; Fig. 2b). The salt KCl was also included to curb precipitation, but this salt had only modest effects at higher Pnt:S100B ratios. Furthermore, KCl had little or effect on Pnt binding to either $Ca^{2+}$–S100B (ITC: $^{Pnt}K_d$=50±5 μM; fluorescence: $^{Pnt}K_d$=44±4 μM) or $Zn^{2+}$,$Ca^{2+}$–S100B (ITC: $^{Pnt}K_d$=35±12 μM; fluorescence: $^{Pnt}K_d$=40±5 μM; Table 2). Pnt binding to each divalent metal ion state of S100B (i.e., $Ca^{2+}$-bound, $Zn^{2+}$,$Ca^{2+}$-bound) was enthalpically favored as judged by negative $\Delta H_{app}$ values measured using ITC (−4.0 to −5.0 kcal/mol; Table 2). The entropic contribution to Pnt binding could also be estimated using the dissociation constant and $\Delta H_{app}$, and in each binding experiment, a thermodynamically favored $T\Delta S$ resulted (+1.0 to +2.1 kcal/mol; Table 2). Such a thermodynamic profile is consistent with productive hydrophobic and hydrogen-bonding interactions upon complex formation.[40,41] When $Zn^{2+}$ binding to $Ca^{2+}$–S100B and to Pnt–$Ca^{2+}$–S100B was examined, the dissociation constants (no drug: $^{Zn}K_d$=94±17 nM; with Pnt: $^{Zn}K_d$=134±9 nM) and the thermodynamic signature of $Zn^{2+}$ binding (i.e., $\Delta H_{app}$, $T\Delta S$) were found to be similar to that determined previously in the absence of Pnt.[7]

In summary, the thermodynamic data presented here indicate that there are two independent Pnt binding sites with indistinguishable affinities in the Pnt–$Ca^{2+}$–S100B and Pnt–$Zn^{2+}$,$Ca^{2+}$–S100B drug complexes (Table 2). We also demonstrate that $Zn^{2+}$ had no detectable effect on Pnt binding to $Ca^{2+}$–S100B, whereas Pnt bound to $Ca^{2+}$–S100B slightly decreased the affinity of the protein for $Zn^{2+}$ (<1.3-fold; Table 2).

### NMR studies characterizing Pnt binding to S100B

STD experiments and chemical shift perturbations were measured by NMR to further characterize the binding of Pnt to $Zn^{2+}$,$Ca^{2+}$–S100B in solution; these results were then compared to similar data recorded previously for Pnt binding to $Ca^{2+}$–S100B (Fig. 3).[31] Only small differences were observed in a comparison of STD data for Pnt bound in the Pnt–$Ca^{2+}$–S100B and Pnt–$Zn^{2+}$,$Ca^{2+}$–S100B complexes, indicating that the H2/H5, H3/H6, and α protons of Pnt were saturated by resonances of S100B in the drug binding site of both $Ca^{2+}$–S100B and $Zn^{2+}$,$Ca^{2+}$–S100B (Fig. 3). That little or no STD was observed for the other protons of Pnt (β and γ) indicated that these protons likely face solvent rather than the binding pocket in both S100B–drug complexes (Fig. 3).[42]

Titrations of Pnt into $Ca^{2+}$- and $Ca^{2+}$,$Zn^{2+}$-bound S100B were compared next by monitoring backbone $^1H$–$^{15}N$ correlations in 2D $^1H$–$^{15}N$ heteronuclear single quantum coherence (HSQC) NMR experiments (Fig. 3). In a titration of Pnt into $Ca^{2+}$–S100B, the $^1H$–$^{15}N$ HSQC correlations of S100B shifted (>30 Hz; Fig. 3) for several residues in helix 1 (A9, I11, D12, and F14), loop 2 (L40, S41, L44, and E46), and helix 4 (Q71, M74, A75, V77, S78, V80, A83, H85, E89, and H90), as previously observed.[31] In a similar titration with $Zn^{2+}$,$Ca^{2+}$–S100B plus Pnt, the $^1H$–$^{15}N$ HSQC correlations of S100B shifted (>30 Hz; Fig. 3) for residues in helix 1 (I11, V13, F14, and H15), loop 2 (L40, S41, H42, L44, and E45), and helix 4 (M74, V77, S78, M79, T82, C84, and E91). When results from these two titrations were compared under identical buffer conditions (i.e., as a $\Delta\Delta\delta$; Fig. 3), Pnt binding did not perturb $^1H$–$^{15}N$

correlations for the same residues in $Ca^{2+}$-bound and $Zn^{2+}$,$Ca^{2+}$-bound S100B, nor did several of these perturbations occur to the same extent. These results indicated that Pnt bound to $Ca^{2+}$–S100B differently (i.e., different orientation) and/or affected the conformation of S100B differently than when Pnt bound to $Zn^{2+}$,$Ca^{2+}$–S100B.

## The X-ray structure of $Zn^{2+}$,$Ca^{2+}$–S100B

The structural consequences of $Zn^{2+}$ binding to $Ca^{2+}$–S100B was important to characterize because of its potential effect on binding specific protein targets such as p53 and/or small-molecule inhibitors such as Pnt.[7,8] With this in mind, the 1.88-Å-resolution X-ray crystal structure for $Zn^{2+}$,$Ca^{2+}$–S100B was solved and compared to that of $Ca^{2+}$–S100B[43,44] (Fig. 5). The final asymmetric unit consisted of 90 residues (Met0 to Glu89), 2 calcium ions, 1 zinc ion, and 51 water molecules. The biologically significant model is a dimer composed of the asymmetric unit and a crystallographic symmetry mate. Nearly all of the residues of $Zn^{2+}$,$Ca^{2+}$–S100B were in the most favorable region of the Ramachandran plot (95.2%) with the remaining residues (4.8%) falling into the allowed region (Table 1; Fig. 4a).

The global fold of $Zn^{2+}$,$Ca^{2+}$–S100B was similar to that reported previously for $Ca^{2+}$–S100B,[43,44] the NMR structure of $Zn^{2+}$,$Ca^{2+}$–S100B,[8] and several other $Ca^{2+}$-loaded S100 proteins.[2,5] Specifically, each subunit of $Zn^{2+}$,$Ca^{2+}$–S100B contained four helices (helix 1, S1–G19; helix 2, K28–L40; helix 3, E49–D61; helix 4, D69–F88) and one small antiparallel β-sheet (strand 1, K26–K28; strand 2, D69–E67) with the dimer interface aligned as a symmetric X-type four-helix bundle comprising helices 1, 1′ and 4, 4′, respectively (Fig. 4a).

As with $Ca^{2+}$–S100B,[43,44] each S100B subunit in $Zn^{2+}$,$Ca^{2+}$–S100B has two $Ca^{2+}$-loaded helix–loop–helix EF hands including an “S100-type” or “pseudo” EF hand comprising helices 1 and 2 and loop 1 and a “typical” EF hand with 12 residues contributed by helices 3 and 4 and loop 3 (Fig. 4). The residues that coordinate calcium in $Zn^{2+}$,$Ca^{2+}$–S100B were found to be the same as those reported previously for $Ca^{2+}$–S100B[44] with minimal differences (<0.3 Å) in coordinate distances (Table 3; Fig. 4). Specifically, calcium coordination in the S100 hand of $Zn^{2+}$,$Ca^{2+}$–S100B was from four backbone carbonyl oxygen atoms including Ser18 (*X* position), Glu21 (*Y* position), Asp23 (*Z* position), and Lys26 (−*Y* position); a water molecule (−*X* position); and the two side-chain carboxylate oxygen atoms of Glu31 (−*Z* position; bidentate ligand). In the typical EF hand, calcium was coordinated by side-chain carboxylate oxygen atoms of Asp61 (*X*-position), Asp63 (*Y*-position), and Asp65 (*Z* position); the backbone carbonyl of Glu67 (−*Y* position); a water molecule (−*X* position); and two side-chain carboxylate oxygen atoms of Glu72 (−*Z* position; bidentate ligand) (Fig. 4b). As discussed previously,[45] a side-chain carboxylate oxygen atom of Glu67 formed a hydrogen bond with a water molecule coorinated to calcium at the −*X* position of the pseudo-EF hand in $Zn^{2+}$,$Ca^{2+}$–S100B (Fig. 4). Importantly, the orientation of helix 3 with respect to helix 4 was found to be in the “open” position in the structures of both $Ca^{2+}$–S100B ($^{X\text{-}ray}\Omega_{3/4}$ =109.9; $^{NMR}\Omega_{3/4}$ = 106 ± 4) and $Zn^{2+}$,$Ca^{2+}$-loaded S100B ($^{X\text{-}ray}\Omega_{3/4}$ = 109.4; $^{NMR}\Omega_{3/4}$ = 118 ± 2), as necessary for binding protein targets such as p53, hdm4, and CapZ (Figs. 1 and 4; Table 4).[8,30,43,44] A slight difference (~9°) in the relative orientation of helices 3 and 4 was observed in the X-ray structure as compared to the NMR structure of $Zn^{2+}$,$Ca^{2+}$–S100B.[8] Such a difference may reflect subtle structural differences in solution *versus* the crystalline state since residual dipolar couplings measured for backbone amide–proton correlations were in better agreement with the NMR family of structures (*Q*-factor<0.3) than with the X-ray structure (*Q*-factor>0.4).[8] Nonetheless, both the NMR and X-ray structures of $Ca^{2+}$–S100B and $Zn^{2+}$,$Ca^{2+}$–S100B should be useful for engineering novel inhibitors of S100B–target protein interactions.

## $Zn^{2+}$ coordination in $Zn^{2+}$,$Ca^{2+}$–S100B

Consistent with site-directed mutagenesis and an NMR structure reported previously,[7,8] the X-ray structure of $Zn^{2+}$,$Ca^{2+}$–S100B has two $Zn^{2+}$ ions per dimer coordinated in a symmetric manner by His15/His25 of one S100B subunit and His85/Glu89 of the other subunit (Fig. 4) [†]. The coordination of $Zn^{2+}$ involves a carboxylate oxygen of Glu89 and nitrogen atoms from the three His residues arranged as a slightly distorted tetrahedral with metal–ligand distances ranging from 1.94 to 2.02 Å and coordinate angles (i.e., O–$Zn^{2+}$–N and N–$Zn^{2+}$–N) ranging from 100° to 115° (Fig. 4; Table 3). This coordination geometry is observed in numerous other $Zn^{2+}$ binding proteins including several S100 proteins.[46,47] For the side chain of Glu89, the $Zn^{2+}$ ion is located in the *syn* position with the second carboxylate oxygen atom at a distance of 2.74 Å from $Zn^{2+}$. This second oxygen atom of the Glu89 side chain also contributes somewhat to metal ion coordination as a fifth ligand.

Several residues near the $Zn^{2+}$ binding site (Val13, His15, Gln16, His25, Phe87, and Phe88) were found to have different side-chain orientations (>1.0 Å RMSD) in $Zn^{2+}$,$Ca^{2+}$–S100B when compared to $Ca^{2+}$–S100B (Fig. 5). The one other side chain positioned differently was Gln71, which forms a hydrogen bond to Thr82 in the $Ca^{2+}$-bound structure, but in $Zn^{2+}$,$Ca^{2+}$–S100B, it is on the surface of the protein and distant from Thr82. Another difference in the two structures is that the side chain for one of the residues that coordinates $Zn^{2+}$, Glu89, could not be traced in the electron density map of $Ca^{2+}$–S100B[44]; however, this side chain was readily observed when $Zn^{2+}$ was bound (Figs. 4 and 5). Together, these data indicated that the movement and/or stabilization of residues at or nearby the $Zn^{2+}$ binding site was required for $Zn^{2+}$ to bind $Ca^{2+}$-loaded S100B (Fig. 5).

## Structures of Pnt bound to $Ca^{2+}$–S100B and $Zn^{2+}$,$Ca^{2+}$–S100B

The X-ray structures of Pnt bound to $Ca^{2+}$–S100B and $Zn^{2+}$,$Ca^{2+}$–S100B were solved at 2.15 and 1.85 Å resolution, respectively (Fig. 6; Table 1). The asymmetric unit for the Pnt–$Ca^{2+}$–S100B structure included 90 residues (Met0 to Glu89), 2 calcium ions, 2 Pnt molecules, and 35 water molecules (Fig. 6; Table 1). It was evident from visual inspection of the $2mF_o$–$DF_c$ and $mF_o$–$DF_c$ electron density maps that the only way to accurately model both Pnt molecules (site 1 and site 2) was to place them in two symmetrical and overlapping orientations with each site having partial occupancies (site 1=0.5, site 2=0.5). The occupancies and temperature factors for the two Pnt orientations at site 1 and site 2 were constrained to be identical owing to the fact that the Pnt molecules reside on a crystallographic 2-fold axis. Thus, the interactions between Pnt and each S100B dimer were identical across the 2-fold axis. Furthermore, the electron density for Pnt bound in sites 1 and 2 was well defined (Fig. 6) with reasonable mean *B* values (Å$^2$) for bound Pnt molecules (site 1=53.14, site 2=43.01) that were comparable to those of side-chain atoms defining the drug binding sites [Table 1; mean *B* value (Å$^2$) for side-chain atoms of Asp12, His42, Cys84, Phe87, and Phe88=38.74].

The asymmetric unit for Pnt–$Zn^{2+}$,$Ca^{2+}$–S100B had 91 residues (Met0 to His90), 2 calcium ions, 1 zinc ion, 2 Pnt molecules, and 82 water molecules (Fig. 6; Table 1). As for Pnt–$Ca^{2+}$–S100B, the $2mF_o$–$DF_c$ and $mF_o$–$DF_c$ electron density maps for Pnt bound to $Zn^{2+}$,$Ca^{2+}$–S100B were also on a crystallographic 2-fold axis and modeled with partial occupancies (site 1=0.3, site 2=0.5). The electron density observed for Pnt bound in sites 1 and 2 of $Zn^{2+}$,$Ca^{2+}$–S100B was also well defined (Fig. 6) with mean *B* values (Å$^2$) for the bound drug molecules (site 1=67.52, site 2=49.85) that were only slightly higher than side-chain atoms of residues

[†]In solution, long-range HSQC data indicated that the $N^{\varepsilon 2}$ of both His15 and His85 and the $N^{\delta 1}$ of His25 were available to coordinate zinc,[8] whereas in the X-ray structure, all three of these His residues were found to coordinate $Zn^{2+}$ via $N^{\varepsilon 2}$ (Fig. 4). Attempts to model His25 coordination via $N^{\delta 1}$ were not successful in refinement of the X-ray structure. That the long-range HSQC data for His25 were somewhat broadened in the $Zn^{2+}$,$Ca^{2+}$-bound form provided some indication that His25 is mobile on the chemical shift timescale, perhaps because both $Zn^{2+}$ coordination geometries (via $N^{\delta 1}$ and $N^{\varepsilon 2}$) are possible in solution.

interacting with the drug [Table 1; mean *B* value (Å$^2$) for side-chain atoms of Val8, Ile11, Phe43, Cys84, and Phe87=45.29]. As with the structure of $Zn^{2+}$,$Ca^{2+}$–S100B, nearly all of the residues in Pnt–$Ca^{2+}$–S100B (95.2%) and Pnt–$Zn^{2+}$,$Ca^{2+}$–S100B (96.5%) were in the most favorable region of the Ramachandran plot, with the remaining 4.8% and 3.5% of the residues in the allowed region, respectively (Table 1).

## Description of the Pnt–$Ca^{2+}$–S100B complex

The global fold, interhelical angles, and calcium-ion coordination of S100B in the Pnt–$Ca^{2+}$–S100B complex were very similar to that reported previously for $Ca^{2+}$–S100B[43,44] (Fig. 6; Tables 3-5). However, specific side chains in $Ca^{2+}$–S100B, including those in helix 1 (Glu2, Lys5, Asp12, Val13, and Gln16), loop 2 (Glu45, Glu49, and Gln50), helix 3 (Glu51 and Lys55), and helix 4 (Gln71, Cys84, Glu86, Phe87, and Phe88), significantly changed position (RMSD>1.0 Å) upon the addition of Pnt (Fig. 7)‡. These changes in S100B structure correspond well with the interactions of two Pnt molecules with S100B observed in the $2mF_o$–$DF_c$ and $mF_o$–$DF_c$ electron density maps for Pnt–$Ca^{2+}$–S100B (arbitrarily termed sites 1 and 2). One Pnt binding site was adjacent to a p53 peptide binding site described previously (site 1; Fig. 6).[27,31] The most notable S100B–Pnt interactions in site 1 resulted from hydrophobic stacking of the benzamidine rings of the drug with aromatic side-chain moieties of the protein including Phe88 from the C-terminal loop to ring 1 of Pnt and His42 from the "hinge" region to ring 2 (Fig. 6). For this interaction to occur, the side chain of Phe88 reoriented upon binding Pnt (Fig. 7). The backbone carbonyls of both His42 and Phe43 also lined this Pnt binding site of $Ca^{2+}$–S100B (<4.0 Å). Importantly, the binding of Pnt to site 1 is consistent with solution NMR data, including an unambiguous intermolecular nuclear Overhauser enhancement between protons of Pnt and Phe88 of S100B.[31]

The second Pnt binding site (site 2) of Pnt–$Ca^{2+}$–S100B was located at the dimer interface in a pocket adjacent to residues that coordinate $Zn^{2+}$ (Fig. 6). This Pnt binding site was best defined by a bidentate hydrogen bond from the two carboxylate oxygen atoms of Asp12 to protons of the $-NH_2$ moieties of one benzamidine ring (2.8 and 3.1 Å; Fig. 6). The second benzamidine ring of Pnt was found to be stacked with the aromatic side chain of Phe87 in helix 4′ of the other subunit of S100B. In addition, a potential weak hydrogen bond between the backbone carbonyl of His85 and an $-NH_2$ moiety of the second benzamidine ring of Pnt was identified (3.3 Å; Fig. 6). As found for site 1, side-chain moieties that interact with the drug in site 2 (Asp12 and Phe87) rotated into position upon binding Pnt (Fig. 7). Likewise, side-chain atoms of Ile11 and Cys84 and the backbone carbonyl of Cys84 were also proximal to Pnt in site 2 (<4.0 Å), which may contribute to binding.

## The Pnt–$Zn^{2+}$,$Ca^{2+}$–S100B complex

When the X-ray structures of $Zn^{2+}$,$Ca^{2+}$–S100B and Pnt–$Zn^{2+}$,$Ca^{2+}$–S100B were compared ($^{mainchain}$RMSD=0.52), the global fold, interhelical angles, and calciumion coordination were nearly identical (Figs. 4 and 6; Tables 3-5). The two Pnt binding sites on Pnt–$Zn^{2+}$,$Ca^{2+}$–S100B were evident in the $2mF_o$–$DF_c$ and $mF_o$–$DF_c$ electron density maps of Pnt–$Zn^{2+}$,$Ca^{2+}$–S100B, and the drug binding sites in this complex were located in positions analogous to sites 1 and 2 in Pnt–$Ca^{2+}$–S100B (Fig. 6). As expected, several side chains changed position when Pnt bound to $Zn^{2+}$,$Ca^{2+}$–S100B (RMSDN>1.0 Å) including residues in helix 1 (Val8, Asp12,

‡It could not be ruled out that different crystal lattice contacts in the $Ca^{2+}$–S100B and Pnt–$Ca^{2+}$–S100B structures [$Ca^{2+}$–S100B: K29–E34, 2.66 Å; D54–R20, 2.88 Å; E51–K24, 2.75 Å; N38–D54, 2.88 Å; Pnt–$Ca^{2+}$–S100B: K28–E58(O), 2.63 Å; E21–S62, 2.67 Å; G22 (NH)–S62(O), 2.67 Å] caused the differences in side-chain positioning at and/or nearby residues Lys24, Lys28, Lys29, Glu49, Gln50, Glu51, Lys55, and Glu58 (Fig. 7). Likewise, it could not be ruled out that different crystal lattice contacts in the $Zn^{2+}$,$Ca^{2+}$–S100B and Pnt–Zn ,$Ca^{2+}$–S100B structures [$Zn^{2+}$,$Ca^{2+}$–S100B: K29–E34, 3.11 Å; D54–R20, 2.65 Å; K29–N38, 2.95 Å; N38–D54, 3.02 Å; Pnt–$Zn^{2+}$,$Ca^{2+}$–S100B: K28–E58 (O), 2.73 Å; E21–S62, 2.80 Å; G22(NH)–S62(O), 2.66 Å; K5–E89, 2.70 Å; E2–H90, 2.67 Å] affected side-chain positioning at and/or nearby residues Glu21, Lys28, Lys29, Leu32, Glu34, Lys58, Val53, Glu58, and Phe88 (Fig. 7).

Val13, and Gln16), loop 2 (Lys48), helix 3 (Val53 and Glu58), and helix 4 (Met74, Met79, Cys84, Glu86, and Phe88)[‡]. However, the residues that changed position in $Zn^{2+}$,$Ca^{2+}$–S100B upon the addition of Pnt (Fig. 7d) and/or the magnitude of such changes were notably different when compared to the changes observed in side-chain positioning between Pnt–$Ca^{2+}$–S100B and $Ca^{2+}$–S100B (Fig. 7b and d). Furthermore, the conformation and orientation of Pnt in both binding sites of Pnt–$Zn^{2+}$,$Ca^{2+}$–S100B were different when compared to the X-ray structure of Pnt–$Ca^{2+}$–S100B (Figs. 6 and 7). These results were in agreement with the observation that $Zn^{2+}$ binding to $Ca^{2+}$–S100B reoriented several residues in helices 1 and 4 that interacted with Pnt binding in the absence of $Zn^{2+}$ (Figs. 5 and 7). That Pnt could adapt to this $Zn^{2+}$-induced conformational change and still bind $Zn^{2+}$,$Ca^{2+}$–S100B was a novel and unanticipated finding. Supporting this result, small differences were also found in solution when STD data were compared for Pnt bound to $Ca^{2+}$–S100B *versus* $Zn^{2+}$,$Ca^{2+}$–S100B (<2-fold changes; relative to the largest STD for the α proton; Fig. 3). While the differences in the STD data are not easily quantified,[48] they are consistent with having different Pnt orientations as was observed when the X-ray structures for the two drug complexes are compared.

The Pnt molecule in site 1 of Pnt–$Zn^{2+}$,$Ca^{2+}$–S100B was relatively extended with little or no bending or kink (Figs. 6 and 7) unlike Pnt bound to site 1 of Pnt–$Ca^{2+}$–S100B. Furthermore, the S100B–drug interaction in site 1 involved only one of the two benzamidine rings. This interaction was dominated by π electron stacking[49] in which one benzamidine ring of Pnt was sandwiched in between two aromatic side chains of $Zn^{2+}$,$Ca^{2+}$–S100B (i.e., Phe43 and Phe87; Figs. 6 and 7). Backbone carbonyl oxygen atoms lining the site (<4.0 Å) include those from residues His42, Phe43, and Ala83, which may also contribute to drug binding. In site 2, the Pnt molecule was relatively kinked when compared to drug bound to the analogous site in Pnt–$Ca^{2+}$–S100B. In addition, Pnt no longer formed a bidentate hydrogen bond with the carboxylate oxygen atoms of Asp12. Rather, a new hydrophobic ring stacking interaction was observed between the benzamidine ring and Phe88, which was rotated into this site (from site 1) upon binding $Zn^{2+}$. In addition, a potential weak hydrogen bond between Cys84 and an $-NH_2$ moiety of the benzamidine ring of Pnt was identified (3.2 Å; Fig. 6). Side-chain atoms from other hydrophobic residues are also near Pnt in site 2 of $Zn^{2+}$,$Ca^{2+}$–S100B including those of Val8 and Ile11. Lastly, the differences observed in the conformation and orientation of Pnt in sites 1 and 2 in the two X-ray structures were consistent with solution NMR studies, which showed differences in chemical shift perturbations when titrations of Pnt into $Ca^{2+}$–S100B *versus* $Zn^{2+}$,$Ca^{2+}$–S100B were compared (i.e., as a ΔΔδ; Fig. 4).

## Discussion

S100B functions as a calcium-activated “switch” (Fig. 1) that undergoes a conformational change as necessary to bind and inhibit the tumor suppressor protein p53.[2,30] In addition, S100B binds $Zn^{2+}$ (one per subunit) at a site separate from the two EF-hand calcium-binding loops. It has been proposed that $Zn^{2+}$ binding might be important for the biological activity of S100B.[7,8,10] Because solution NMR studies did not precisely define the coordination geometry of $Zn^{2+}$ bound to S100B, we solved the crystal structure of $Zn^{2+}$,$Ca^{2+}$–S100B (Fig. 4).[7,8] We also obtained details regarding a protein conformational change that was induced by $Zn^{2+}$ binding to $Ca^{2+}$-loaded S100B (Fig. 5), which could be important to consider when inhibiting S100B–target protein interactions. Thus, when the X-ray structures of Pnt–$Ca^{2+}$–S100B and Pnt–$Zn^{2+}$,$Ca^{2+}$–S100B were compared (Figs. 6 and 7), we found that two drug molecules (per S100B subunit) bound sites that were similarly located in the two structures; however, the conformation and orientation of Pnt bound in these two sites were very different (±$Zn^{2+}$). Structural data such as these can now be used to design/synthesize higher-affinity inhibitors that target specific divalent metal ion-bound states of S100B as might be necessary for melanoma where $Ca^{2+}$ and $Zn^{2+}$ levels are unregulated.

## $Zn^{2+}$ binding to S100 proteins

It was predicted that the $Zn^{2+}$ binding site in S100B would be composed of residues from both subunits (subunit 1: His15/His25, subunit 2: His85′/Glu89′).[7,8] This coordination scheme was confirmed by our X-ray crystallographic studies (Fig. 4). When the $Zn^{2+}$ site of S100B [Fig. 4; Protein Data Bank (PDB) code: 3CR2] was compared to other S100 proteins (using S100B numbering), a structurally conserved $Zn^{2+}/Cu^{2+}$ binding site, distinct from the two EF-hand $Ca^{2+}$ binding sites, was also observed for S100A7 ($Zn^{2+}$: His17/Asp24/His86′/His90′; PDB code: 2PSR)[46] and S100A12 ($Cu^{2+}$: His15/Asp25/His85′/His89′; PDB code: 1ODB)[50,51] (Fig. 8). As found here for S100B, four of the five ligands (one side-chain carboxylate oxygen; three His nitrogen atoms) from S100A7 and S100A12 coordinate divalent metal ion in a slightly distorted tetrahedral geometry with similar metal ion–ligand distances (~2 Å). The fifth ligand is at a longer metal ion–ligand distance (>2.5 Å) and is provided by the second side-chain carboxylate oxygen atom of Glu89 in subunit 2 of S100B. In contrast, for S100A7 and S100A12, this more weakly coordinating oxygen ligand was from an aspartate side chain in subunit 1 (S100A7: Asp24, S100A12: Asp25; Fig. 8).

Several other S100 proteins also bind $Zn^{2+}$ including S100A1,[52] S100A2,[53] S100A3,[54] S100A5,[55] S100A6,[56,57] and S100P (low affinity),[58] but these proteins likely coordinate $Zn^{2+}$ differently than observed here for S100B, since there is little sequence homology for the $Zn^{2+}$-liganding residues when compared to S100B, S100A7, or S100A12.[47] For S100A8/A9, it was predicted that the heterodimer coordinates $Zn^{2+}$ in a manner similar to that of S100B, S100A7, and S100A12,[59] and as found here for S100B, $Zn^{2+}$ binding induced a conformational change in the S100A8/A9 heterodimer complex that was distinct from the $Ca^{2+}$-dependent change.[59] Nonetheless, it still remains necessary to directly determine the high-resolution structures for each of these other $Zn^{2+}$ binding S100 proteins to accurately characterize their coordination geometry and structural changes that occur upon binding $Zn^{2+}$.

## The effects of $Zn^{2+}$ on $Ca^{2+}$ and target protein binding to S100B

The biological significance of $Zn^{2+}$ and/or $Cu^{2+}$ binding has not yet been fully elucidated for any S100 protein despite the fact that several of these proteins contain structurally homologous $Zn^{2+}/Cu^{2+}$ binding sites (Fig. 8). It was proposed that antimicrobial activity associated with S100A7 and S100A8/A9 proteins resulted from sequestering free $Zn^{2+}$ and inhibiting $Zn^{2+}$-activated enzymes *in vivo*.[59-61] However, the ability of S100 proteins to compete for free $Zn^{2+}$ is unlikely due to the relatively high dissociation constant of $Zn^{2+}$ from S100 proteins (i.e., ~100 nM; Table 2) as compared with most $Zn^{2+}$-activated enzymes.[62,63]

It is more likely that $Zn^{2+}$ binding contributes to S100 function by modulating their $Ca^{2+}$ and/or target protein interactions as was observed *in vitro* for several S100 proteins.[47] For example, the affinity of S100B for $Ca^{2+}$ is increased by nearly an order of magnitude in the presence of $Zn^{2+}$.[9,10] One possibility for this observation was that Zn2+ binding caused a conformational change such that $Ca^{2+}$ ions in the typical and pseudo-EF hands were more optimally coordinated. Such an explanation was ruled out here since no change in calcium coordination in S100B was observed in either EF-hand domain when the crystal structures of $Ca^{2+}$–S100B and $Zn^{2+}$,$Ca^{2+}$–S100B were compared (Fig. 5; Tables 3-5). Another possibility is that perhaps $Zn^{2+}$ binding to apo–S100B contributes to increased $Ca^{2+}$ binding; however, this and several other alternate mechanistic explanation(s) for how $Zn^{2+}$ binding increases $Ca^{2+}$ binding affinity must now be explored (i.e., effects on $K_{on}$, conformational equilibriums, protein dynamics, etc.).

The binding of $Zn^{2+}$ to $Ca^{2+}$–S100B has also been reported to increase the affinity of several protein targets for S100B including CapZ,[13] the AHNAK protein,[15] and the tau protein.[14] Likewise, target protein interactions involving S100A6 and S100A11 were of higher affinity

when these S100 proteins were bound to $Zn^{2+}$.[12] For S100A1, $Zn^{2+}$ binding provided more than a 30-fold enhancement in binding the protein target twitchen kinase[52] and raised the question of whether $Zn^{2+}$ binding modulates S100 protein function as part of a more general mechanism *in vivo* for this family of proteins.[4,47] Close examination of conformational change that $Zn^{2+}$ induced in $Ca^{2+}$–S100B (Fig. 5) together with the availability of structural data for several target peptide complexes of S100B can provide some insight for how this might occur. For example, the TRTK-12 peptide binds $Zn^{2+}$,$Ca^{2+}$–S100B an order of magnitude more tightly than $Ca^{2+}$–S100B.[13] In this S100B–peptide complex, several residues that interact directly with TRTK-12 including Phe87 and Phe88,[64] were found to be reoriented when $Zn^{2+}$ bound to $Ca^{2+}$–S100B (Fig. 5). Perhaps this $Zn^{2+}$-induced conformational change in $Ca^{2+}$–S100B at or nearby the TRTK-12 binding site introduced additional and/or more energetically favorable interaction(s) with the TRTK-12 peptide, although such an explanation needs to be verified by directly examining the structure of $Zn^{2+}$,$Ca^{2+}$–S100B bound to a target protein/peptide.

## The structures of Pnt bound to $Ca^{2+}$–-S100B (±$Zn^{2+}$)

As part of an effort to inhibit S100B, the Food and Drug Administration-approved drug Pnt was characterized by NMR and found to interact with aromatic residues in helix 4 and the C-terminal loop of $Ca^{2+}$-loaded S100B.[31] To pursue this S100B–drug interaction further, we determined the X-ray crystal structures of Pnt bound to $Ca^{2+}$- and $Zn^{2+}$, $Ca^{2+}$-bound S100B in this study. In both complexes, it was discovered that S100B bound two Pnt molecules per S100B subunit with one molecule located adjacent to the p53 peptide binding site (termed site 1), as predicted previously.[31] The second Pnt molecule was found to bind to a separate site (site 2), adjacent to a well-characterized $Zn^{2+}$ binding site on S100B.[8] Pnt bound to site 2 was found to interact with residues in helix 1 of one subunit and helix 4′ of the second subunit but had no direct interaction with $Zn^{2+}$. Nonetheless, a change in the relative orientation of the drug in both sites 1 and 2 was observed when $Zn^{2+}$ was bound (Fig. 6).

Next, the dependence of calcium on Pnt binding to S100B was examined in detail by comparing the three-dimensional structures of apo–S100B, Ca2+–S100B, Pnt–$Ca^{2+}$–S100B, and Pnt–$Zn^{2+}$,Ca*2*+–S100B (Fig. 9). As observed previously,[43] the relative orientation of helix 3, helix 4, and the hinge region (loop 2) is quite different in the apo- and $Ca^{2+}$-bound states of S100B (Figs. 1 and 9), which could explain the calcium-dependent binding of Pnt to sites 1 and 2. Furthermore, in the absence of calcium, a large portion of both Pnt sites 1 and 2 was occluded by several side chains of S100B including Glu46 and His90 (Fig. 9). As a result, two residues (His42 and Phe88) that approach each other in $Ca^{2+}$–S100B (8 Å) and then ring stack with Pnt in site 1 of the Pnt–$Ca^{2+}$–S100B complex are completely separated in the apo state (>16 Å; Fig. 9). In site 2, additional changes are observed upon the addition of calcium. Specifically, in the apo structure, His90 is in a location that occludes much of site 2, and Phe87, another important residue for binding Pnt in site 2, is ring stacked with Phe88 and unavailable to interact with the drug. Upon binding Ca , the position of His90 becomes uncertain, likely due to dynamic properties of the protein, and a drug-binding pocket appears, which includes Asp12, a residue that forms a bidentate hydrogen bond with the amidine moiety of Pnt. Ring stacking between Phe87 and Phe88 is also disrupted when Pnt binds $Ca^{2+}$–S100B such that Phe88 interacts with Pnt in site 1 and Phe87 interacts with Pnt in site 2. While additional protein conformational changes occur upon the addition of $Zn^{2+}$, Pnt molecules are remarkably adaptive and still bind both sites 1 and 2 with an affinity similar to that when only $Ca^{2+}$ was present (Figs. 6 and 9; Table 2).

## Summary

Overall, a comparison of the X-ray crystal structures of $Ca^{2+}$–S100B and $Zn^{2+}$,$Ca^{2+}$–S100B showed for the first time that $Zn^{2+}$ binding had no discernable effect on $Ca^{2+}$ ion coordination

in either the pseudo- or the typical EF-hand calcium-binding domains. Although the binding of $Zn^{2+}$ did induce a conformational change in $Ca^{2+}$–S100B that affected the protein's structure in regions where target proteins bind (i.e., for residues at or nearby Phe87 and Phe88 in helix 4). These differences in S100B structure, in turn, affected the conformation and orientation of two Pnt molecules bound to analogous sites on $Ca^{2+}$–S100B and $Zn^{2+}$,$Ca^{2+}$–S100B. Together, the structural studies presented here will likely impact the design of new S100B inhibitors, which could have therapeutic value for the treatment of cancers with elevated S100B such as malignant melanoma.

## Materials and Methods

### Materials

All chemicals and reagents were American Chemical Society grade or higher and typically purchased from Sigma-Aldrich unless otherwise indicated. $^{15}NH_4Cl$ was purchased from Cambridge Isotope Laboratories (Andover, MA). All buffers were passed through Chelex-100 resin to remove trace metals prior to use.

### Bacterial expression and purification of the wild-type S100B

Recombinant S100B protein (rat, bovine) was expressed in *Escherichia coli* [HMS174(DE3) strain] and purified as previously described.[43] Yields of S100B protein were typically 20–30 mg of purified protein per liter of bacterial culture. For NMR experiments, S100B protein was prepared using defined media that included $^{15}N$-labeled $NH_4Cl$ as the only nitrogen source.[43]

### NMR spectroscopy

Purified $^{15}N$-labeled S100B was dialyzed against 0.1 mM 2-{[2-hydroxy-1,1-bis (hydroxymethyl)ethyl] amino}ethanesulfonic acid (Tes), pH 7.2, and 0.05 mM DTT; lyophilized; and hydrated in a small aliquot of $ddH_2O$ (deionized and doubly distilled $H_2O$) and stored at −80 or −20 °C. The $Ca^{2+}$-loaded S100B–Pnt NMR sample was prepared in a manner similar to that previously described[31] and contained 0.5 mM S100B subunit concentration, 0.5–0.75 mM Pnt, 0.34 mM $NaN_3$, 15 mM NaCl, 0–5% $d_6$-dimethyl sulfoxide, 10–15 mM $CaCl_2$, 10% $D_2O$, and 10 mM Tes buffer and adjusted to pH 7.2 with HCl. As described previously, 0.7 mM ZnAc was added to $Ca^{2+}$–S100B, and the resonance assignments determined previously for $Zn^{2+}$,$Ca^{2+}$–S100B were confirmed.[7] These chemical shift assignments were then used as a starting point during titrations with Pnt to assign the 2D $^1H$–$^{15}N$ HSQC spectra of S100B in the Pnt–$Zn^{2+}$, $Ca^{2+}$–S100B complex.[65]

Group epitope mapping via STD NMR was completed for the Pnt–$Zn^{2+}$,$Ca^{2+}$–S100B complex in a manner similar to that described previously for Pnt–$Ca^{2+}$–S100B.[66] Specifically, during the 2-s presaturation pulse, the onresonance irradiation of the protein was performed at a chemical shift of −0.4 ppm and the off-resonance irradiation was applied at 30 ppm, where no protein signals were present. As a control, the STD experiments were collected in the absence of a $T_{1\rho}$ filter, and as expected, the 1D spectrum of holo–S100B was fully restored. The final sample contained either 60 μM ZnAc or no ZnAc and 50 μM S100B, 500 μM Pnt, 10 mM $CaCl_2$, 5% $d_6$-dimethyl sulfoxide, 99.98% $D_2O$, 15 mM NaCl, 100 mM KCl, 0.34 mM $NaN_3$, and 10 mM Tris-$d_{11}$, pH 7.2. The STD data were collected at 25 °C to achieve more efficient saturation of the protein. Proton assignments of Pnt were confirmed in the above conditions in the absence and presence of S100B using 2D total correlated spectroscopy experiments.[67]

HSQC NMR data were collected at 37 °C with a Bruker Avance III 600 (600.13 MHz for protons) or with an Avance 800 US2 (800.27 MHz for protons) NMRspectrometer both equipped with pulsed-field gradients, four frequency channels, and triple-resonance, *z*-axis

gradient cryogenic probes.[65] Data were processed with NMRPipe,[68] and proton chemical shifts were reported with respect to the $H_2O$ or HDO signal taken as 4.658 ppm relative to external trimethylsilylpropionic acid (0.0 ppm). The $^{15}N$ chemical shifts were indirectly referenced as previously described using the following ratio of the zero-point frequency: 0.10132905 for $^{15}N$ to $^{1}H$.[69-71]

## Thermodynamic binding studies

The calcium-dependent interaction between S100B and Pnt was monitored in titrations of S100B into Pnt (100 μM) and by measuring increases in Pnt fluorescence intensity at 345 nm ($\lambda_{ex}$=262 and 299 nm). The fluorescence data were collected on a Varian Cary Eclipse fluorescence spectrophotometer with the temperature maintained at 37 °C using a circulating constant-temperature bath. All measurements were performed in quartz cuvettes with buffer containing 10 mM Tes, pH 7.2, 15 mM NaCl, 0–100 mM KCl, 0–10 mM $CaCl_2$, and 0–500 μM ZnAc. Binding of Pnt to $Ca^{2+}$–S100B and $Zn^{2+}$,$Ca^{2+}$–S100B was also examined via ITC with a VP-ITC titration microcalorimeter (MicroCal, Inc., Northampton, MA), as described previously.[7] For ITC, all S100B and Pnt solutions were degassed under vacuum for 5 min and equilibrated at 37 °C prior to use. The reference cell contained $ddH_2O$, and the sample cell (1.4 mL) contained 10–50 mM Tes at pH 7.2, 15 mM NaCl, 0–100 mM KCl, 10 mM $CaCl_2$, 0–100 μM $ZnCl_2$, and 0.1 mM S100B. Upon equilibration, a 2.5- to 5-mM Pnt solution prepared in the same buffer as above (without S100B) was injected in 5-μL aliquots with a 300-s interval between each injection. In all titrations containing $Zn^{2+}$, the $Zn^{2+}$-to-S100B subunit ratio did not exceed 1:1 to avoid precipitation. The resulting titration curves were corrected for the protein-free buffer control and analyzed using the Origin for ITC software supplied by MicroCal, Inc.

## Protein crystallization

Bovine S100B protein was dialyzed into buffer (0.1 mM Tes, pH 7.2, and 0.05 mM DTT), lyophilized, dissolved in $ddH_2O$ to 80–100 mg/mL (~8–10 mM subunit concentration), and stored frozen. Diffraction quality crystals for the $Zn^{2+}$,$Ca^{2+}$–S100B complex were obtained by sitting drop vapor diffusion at 22 °C by mixing 2 μL of S100B protein (40 mg/mL S100B, 7.5 mM $CaCl_2$, 3.8 mM $ZnAc_2$, and 20 mM cacodylate buffer, pH 7.2) with 2 μL of reservoir solution [7.5 mM $CaCl_2$, 0.1 M cacodylate buffer, pH 6.5, and 28% polyethylene glycol (PEG) 3350] and equilibrating for 2–3 days. After crystals formed, they were cryoprotected in a harvest solution (7.5 mM $CaCl_2$, 3.8 mM $ZnAc_2$, 0.1 M cacodylate buffer, pH 6.5, 30% PEG3350, and 5% glycerol) for 30–60 s and then flashcooled in liquid nitrogen. The Pnt–$Ca^{2+}$–S100B and Pnt–$Ca^{2+}$,$Zn^{2+}$–S100B complexes were crystallized in a similar manner using complex-specific protein buffers (Pnt–$Ca^{2+}$–S100B: 40 mg/mL S100B, 7.5 mM $CaCl_2$, 3.8 mM Pnt, and 20 mM cacodylate buffer, pH 7.2; Pnt–$Ca^{2+}$,$Zn^{2+}$–S100B: 40 mg/mL S100B, 7.5 mM $CaCl_2$, 3.8 mM $ZnAc_2$, 3.8 mM Pnt, and 20 mM cacodylate buffer, pH 7.2), reservoir solutions (Pnt–$Ca^{2+}$–S100B: 7.5 mM $CaCl_2$, 0.1 M cacodylate buffer, pH 7.8, and 26% PEG3350; Pnt–$Ca^{2+}$,$Zn^{2+}$–S100B: 7.5mM$CaCl_2$, 0.1Mcacodylate buffer, pH 7.6, and 22% PEG3350), and harvest solutions (Pnt–$Ca^{2+}$–S100B: 7.5 mM $CaCl_2$, 3.8 mM Pnt, 0.1 M cacodylate buffer, pH 7.8, 28% PEG3350, and 5% glycerol; Pnt–$Ca^{2+}$,$Zn^{2+}$–S100B: 7.5 mM $CaCl_2$, 3.8 mM $ZnAc_2$, 3.8 mM Pnt, 0.1 M cacodylate buffer, pH 7.6, 24% PEG3350, and 5% glycerol). Space groups and unit cell parameters are given in Table 1. Each of the above crystal forms had one S100B subunit in the asymmetric unit.

## X-ray data collection, model building, and refinement

X-ray data for the $Zn^{2+}$,$Ca^{2+}$–S100B and Pnt–$Zn^{2+}$,$Ca^{2+}$–S100B crystals were collected remotely at the 9-1 beamline (Stanford Synchrotron Radiation Laboratory, Menlo Park, CA) using an ADSC Quantum-315R CCD detector (Area Detector Systems Corporation, Poway,

CA). X-ray data for Pnt–$Ca^{2+}$–S100B were collected at 100 K using an in-house X-ray generator (MSC Micromax 7; Rigaku Texas, USA) and a Raxis-4++ image plate detector (Rigaku Texas). The reflection intensities were integrated and scaled with the HKL2000 suite of computer programs.[72] The crystals of $Zn^{2+}$,$Ca^{2+}$–S100B, Pnt–$Ca^{2+}$–S100B, and Pnt–$Zn^{2+}$,$Ca^{2+}$–S100B diffracted to 1.88, 2.15, and 1.85 Å resolution, respectively. Preliminary phases were obtained via molecular replacement techniques using the structure of $Ca^{2+}$-bound S100B (PDB code: 1MHO;[44]) as a search model and the computer program Molrep and/or Phaser from the CCP4 program suite.[73] Model building and refinement of S100B were completed using REFMAC5 and COOT.[74,75] The locations of the two Pnt molecules and several water molecules were determined by visual inspection of $2mF_o–DF_c$ and $mF_o–DF_c$ electron density maps with the program COOT.[75] It was evident from visual inspection of the $2mF_o–DF_c$ and $mF_o–DF_c$ electron density maps that the only way to accurately model the bound Pnt in site 1 was to place the molecule in two overlapping orientations, each with partial occupancy. We determined the final occupancy for Pnt orientation in the $Ca^{2+}$–S100B and $Zn^{2+}$,$Ca^{2+}$–S100B of site 1 to be 0.5 and 0.3, giving a total occupancy for Pnt at that site of 1.0 and 0.6, respectively. The occupancy was set manually and the value was chosen because higher or lower values resulted in positive or negative difference density around the drug. The occupancies and temperature factors for the two Pnt orientations at site 1 were constrained to be identical owing to the fact that the Pnt resides on a crystallographic 2-fold axis. Modeling of Pnt at site 2 was similar to that at site 1, with two molecules having overlapping orientations with occupancies of 0.5, resulting in a total occupancy of 1.0 for Pnt in site 2. As it turned out, the occupancies in site 1 varied while those in site 2 were found to be similar for both Pnt–S100B complex structures (i.e., Pnt–$Ca^{2+}$–S100B and Pnt–$Zn^{2+}$,$Ca^{2+}$–S100B), whereas the temperature factors for the Pnt molecules at those sites varied between the two complexes (Table 1). The stereochemistry was checked with the programs WHATCHECK and PROCHEK,[76,77] and interhelix angles and distances were calculated using the programs INTERHLX,[78] VGM,[78] and IHA.[79] The quaternary structure and accessible surface areas were analyzed using the PISA server[§]. Figures were generated with the program PyMOL[‖].

## Acknowledgements

This work was supported by grants from the National Institutes of Health [GM58888 and CA107331 (to D.J.W.)], the American Cancer Society [CDD107745 (to D.J.W.)], and The University of Maryland Drug Design Center.

## Abbreviations used

Pnt, pentamidine; ITC, isothermal titration calorimetry; PEG, polyethylene glycol; HSQC, heteronuclear single quantum coherence; STD, saturation transfer difference; Tes, 2-{[2-hydroxy-1,1-bis (hydroxymethyl)ethyl]amino}ethanesulfonic acid; $ddH_2O$, deionized and doubly distilled $H_2O$; PDB, Protein Data Bank; VGM, vector geometry mapping.

## References

1. Moore B. A soluble protein characteristic of the nervous system. Biochem. Biophys. Res. Commun 1965;1:739–744. [PubMed: 4953930]
2. Weber, DJ.; Rustandi, RR.; Carrier, F.; Zimmer, DB. Interaction of dimeric S100B(ββ) with the tumor suppressor protein: a model for Ca-dependent S100-target protein interactions. In: Pochet, R., editor. The Molecular Basis of Calcium Action in Biology and Medicine. Kluwer Academic Publishers; Dordrecht, The Netherlands: 2000.

[§]http://www.ebi.ac.uk/msd-srv/prot_int/cgi-bin/piserver
[‖]http://www.pymol.org

3. Donato R. Intracellular and extracellular roles of S100 proteins. Microsc. Res. Tech 2003;60:540–551. [PubMed: 12645002]
4. Heizmann CW. The multifunctional S100 protein family. Methods Mol. Biol 2002;172:69–80. [PubMed: 11833360]
5. Santamaria-Kisiel L, Rintala-Dempsey AC, Shaw GS. Calcium-dependent and -independent interactions of the S100 protein family. Biochem. J 2006;396:201–214. [PubMed: 16683912]
6. Rustandi RR, Drohat AC, Baldisseri DM, Wilder PT, Weber DJ. The $Ca^{2+}$-dependent interaction of S100B with a peptide derived from p53. Biochemistry 1998;37:1951–1960. [PubMed: 9485322]
7. Wilder PT, Baldisseri DM, Udan R, Vallely KM, Weber DJ. Location of the Zn(2+)-binding site on S100B as determined by NMR spectroscopy and site-directed mutagenesis. Biochemistry 2003;42:13410–13421. [PubMed: 14621986]
8. Wilder PT, Varney KM, Weiss MB, Gitti RK, Weber DJ. Solution structure of zinc- and calcium-bound rat S100B as determined by nuclear magnetic resonance spectroscopy. Biochemistry 2005;44:5690–5702. [PubMed: 15823027]
9. Baudier J, Gerard D. Ions binding to S100 proteins: structural changes induced by calcium and zinc on S100a and S100b proteins. Biochemistry 1983;22:3360–3369. [PubMed: 6615778]
10. Baudier J, Glasser N, Gerard D. Ions binding to S100 proteins. I. Calcium- and zinc-binding properties of bovine brain S100αα, S100a (αβ), and S100b (ββ) protein: $Zn^{2+}$ regulates $Ca^{2+}$ binding on S100b protein. J. Biol. Chem 1986;261:8192–8203. [PubMed: 3722149]
11. Baudier J, Haglid K, Haiech J, Gerard D. Zinc ion binding to human brain calcium binding proteins, calmodulin and S100b protein. Biochem. Biophys. Res. Commun 1983;114:1138–1146. [PubMed: 6615509]
12. Deloulme JC, Assard N, Mbele GO, Mangin C, Kuwano R, Baudier J. S100A6 and S100A11 are specific targets of the calcium- and zinc-binding S100B protein *in vivo*. J. Biol. Chem 2000;275:35302–35310. [PubMed: 10913138]
13. Barber KR, McClintock KA, Jamieson GA Jr, Dimlich RV, Shaw GS. Specificity and $Zn^{2+}$ enhancement of the S100B binding epitope TRTK-12. J. Biol. Chem 1999;274:1502–1508. [PubMed: 9880526]
14. Baudier J, Cole RD. Interactions between the microtubule-associated tau proteins and S100b regulate tau phosphorylation by the $Ca^{2+}$/calmodulin-dependent protein kinase II. J. Biol. Chem 1988;263:5876–5883. [PubMed: 2833519]
15. Gentil BJ, Delphin C, Mbele GO, Deloulme JC, Ferro M, Garin J, Baudier J. The giant protein AHNAK is a specific target for the calcium-and zinc-binding S100B protein: potential implications for $Ca^{2+}$ homeostasis regulation by S100B. J. Biol. Chem 2001;276:23253–23261. [PubMed: 11312263]
16. Zimmer DB, Cornwall EH, Landar A, Song W. The S100 protein family: history, function, and expression. Brain Res. Bull 1995;37:417–429. [PubMed: 7620916]
17. Hansson LO, Vonschoultz E, Djureen E, Hansson J, Nilsson B, Ringborg U. Prognostic value of serum analyses of S100 protein beta in malignant melanoma. Anticancer Res 1997;17:3071–3073. [PubMed: 9329604]
18. Maelandsmo GM, Florenes VA, Mellingsaeter T, Hovig E, Kerbel RS, Fodstad O. Differential expression patterns of S100A2, S100A4 and S100A6 during progression of human malignant melanoma. Int. J. Cancer 1997;74:464–469. [PubMed: 9291441]
19. Boni R, Heizmann CW, Doguoglu A, Ilg EC, Schafer BW, Dummer R, Burg G. $Ca^{2+}$-binding proteins S100A6 and S100B in primary cutaneous melanoma. J. Cutaneous Pathol 1997;24:76–80.
20. Camby I, Lefranc F, Titeca G, Neuci S, Fastrez M, Dedecken L, et al. Differential expression of S100 calcium-binding proteins characterizes distinct clinical entities in both WHO grade II and III astrocytic tumours. Neuropathol. Appl. Neurobiol 2000;26:76–90. [PubMed: 10736069]
21. Camby I, Nagy N, Lopes MB, Schafer BW, Maurage CA, Ruchoux MM, et al. Supratentorial pilocytic astrocytomas, astrocytomas, anaplastic astrocytomas and glioblastomas are characterized by a differential expression of S100 proteins. Brain Pathol 1999;9:1–19. [PubMed: 9989446]
22. Davey GE, Murmann P, Heizmann CW. Intracellular $Ca^{2+}$ and $Zn^{2+}$ levels regulate the alternative cell density-dependent secretion of S100B in human glioblastoma cells. J. Biol. Chem 2001;276:30819–30826. [PubMed: 11402046]

23. Hauschild A, Engel G, Brenner W, Glaser R, Monig H, Henze E, Christophers E. Predictive value of serum S100B for monitoring patients with metastatic melanoma during chemotherapy and/or immunotherapy. Br. J. Dermatol 1999;140:1065–1071. [PubMed: 10354072]
24. Hauschild A, Engel G, Brenner W, Glaser R, Monig H, Henze E, Christophers E. S100B protein detection in serum is a significant prognostic factor in metastatic melanoma. Oncology 1999;56:338–344. [PubMed: 10343200]
25. Hauschild A, Michaelsen J, Brenner W, Rudolph P, Glaser R, Henze E, Christophers E. Prognostic significance of serum S100B detection compared with routine blood parameters in advanced metastatic melanoma patients. Melanoma Res 1999;9:155–161. [PubMed: 10380938]
26. Baudier J, Delphin C, Grunwald D, Khochbin S, Lawrence JJ. Characterization of the tumor suppressor protein p53 as a protein kinase C substrate and an S100b-binding protein. Proc. Natl Acad. Sci. USA 1992;8:11627–11631. [PubMed: 1454855]
27. Rustandi RR, Baldisseri DM, Weber DJ. Structure of the negative regulatory domain of p53 bound to S100B. Nat. Struct. Biol 2000;7:570–574. [PubMed: 10876243]
28. Delphin C, Ronjat M, Deloulme JC, Garin G, Debussche L, Higashimoto Y, et al. Calcium-dependent interaction of S100B with the C-terminal domain of the tumor suppressor p53. J. Biol. Chem 1999;274:10539–10544. [PubMed: 10187847]
29. Lin J, Yang Q, Yan Z, Markowitz J, Wilder PT, Carrier F, Weber DJ. Inhibiting S100B restores p53 levels in primary malignant melanoma cancer cells. J. Biol. Chem 2004;279:34071–34077. [PubMed: 15178678]
30. Wilder PT, Lin J, Bair CL, Charpentier TH, Yang D, Liriano M, et al. Recognition of the tumor suppressor protein p53 and other protein targets by the calcium-binding protein S100B. Biochim. Biophys. Acta 2006;1763:1284–1297. [PubMed: 17010455]
31. Markowitz J, Chen I, Gitti R, Baldisseri DM, Pan Y, Udan R, et al. Identification and characterization of small molecule inhibitors of the calcium-dependent S100B–p53 tumor suppressor interaction. J. Med. Chem 2004;47:5085–5093. [PubMed: 15456252]
32. Markowitz J, Mackerell AD Jr, Carrier F, Charpentier TH, Weber DJ. Design of inhibitors for S100B. Curr. Top. Med. Chem 2005;5:1093–1108. [PubMed: 16248785]
33. Markowitz J, MacKerell AD Jr, Weber DJ. A search for inhibitors of S100B, a member of the S100 family of calcium-binding proteins. Mini Rev. Med. Chem 2007;7:609–616. [PubMed: 17584159]
34. Borovansky J, Riley PA, Vrankova E, Necas E. The effect of zinc on mouse melanoma growth *in vitro* and *in vivo*. Neoplasma 1985;32:401–406. [PubMed: 4047252]
35. Gorodetsky R, Sheskin J, Weinreb A. Iron, copper, and zinc concentrations in normal skin and in various nonmalignant and malignant lesions. Int. J. Dermatol 1986;25:440–445. [PubMed: 3771040]
36. Ros-Bullon MR, Sanchez-Pedreno P, Martinez-Liarte JH. Serum zinc levels are increased in melanoma patients. Melanoma Res 1998;8:273–277. [PubMed: 9664150]
37. Prasad KN, Ahrens CR, Barrett JM. Homeostasis of zinc and iron in mouse B16 melanoma. Cancer Res 1969;2:1019–1023. [PubMed: 5781094]
38. Lin J, Blake M, Tang C, Zimmer D, Rustandi RR, Weber DJ, Carrier F. Inhibition of p53 transcriptional activity by the S100B calcium-binding protein. J. Biol. Chem 2001;276:35037–35041. [PubMed: 11454863]
39. Wilson D, Varigos G, Ackland ML. Apoptosis may underlie the pathology of zinc-deficient skin. Immunol. Cell Biol 2006;84:28–37. [PubMed: 16405650]
40. Velazquez-Campoy A, Todd MJ, Freire E. HIV-1 protease inhibitors: enthalpic versus entropic optimization of the binding affinity. Biochemistry 2000;3:2201–2207. [PubMed: 10694385]
41. Jelesarov I, Bosshard HR. Isothermal titration calorimetry and differential scanning calorimetry as complementary tools to investigate the energetics of biomolecular recognition. J. Mol. Recognit 1999;12:3–18. [PubMed: 10398392]
42. Meyer B, Klein J, Mayer M, Meinecke R, Moller H, Neffe A, et al. Saturation transfer difference NMR spectroscopy for identifying ligand epitopes and binding specificities. Ernst Schering Res. Found. Workshop 2004;44:149–167. [PubMed: 14579779]
43. Drohat AC, Baldisseri DM, Rustandi RR, Weber DJ. Solution structure of calcium-bound rat S100B as determined by nuclear magnetic resonance spectroscopy. Biochemistry 1998;37:2729–2740. [PubMed: 9485423]

44. Matsumura H, Shiba T, Inoue T, Harada S, Kai Y. A novel mode of target recognition suggested by the 2.0 Å structure of holo S100B from bovine brain. Structure 1998;6:233–241. [PubMed: 9519413]
45. Otterbein LR, Kordowska J, Witte-Hoffmann C, Wang CL, Dominguez R. Crystal structures of S100A6 in the Ca(2+)-free and Ca(2+)-bound states: the calcium sensor mechanism of S100 proteins revealed at atomic resolution. Structure 2002;10:557–567. [PubMed: 11937060]
46. Brodersen DE, Nyborg J, Kjeldgaard M. Zinc-binding site of an S100 protein revealed. Two crystal structures of $Ca^{2+}$-bound human psoriasin (S100A7) in the $Zn^{2+}$-loaded and $Zn^{2+}$-free states. Biochemistry 1999;38:1695–1704. [PubMed: 10026247]
47. Heizmann CW, Cox JA. New perspectives on S100 proteins: a multi-functional Ca(2+)-, Zn(2+)- and Cu(2+)-binding protein family. BioMetals 1998;11:383–397. [PubMed: 10191501]
48. Yan J, Kline AD, Mo H, Shapiro MJ, Zartler ER. The effect of relaxation on the epitope mapping by saturation transfer difference NMR. J. Magn. Reson 2003;163:270–276. [PubMed: 12914842]
49. Burley SK, Petsko GA. Aromatic-aromatic interaction: a mechanism of protein structure stabilization. Science 1985;22:23–28. [PubMed: 3892686]
50. Moroz OV, Antson AA, Grist SJ, Maitland NJ, Dodson GG, Wilson KS, et al. Structure of the human S100A12–copper complex: implications for host-parasite defence. Acta Crystallogr., Sect. D: Biol. Crystallogr 2003;5:859–867. [PubMed: 12777802]
51. Moroz OV, Dodson GG, Wilson KS, Lukanidin E, Bronstein IB. Multiple structural states of S100A12: a key to its functional diversity. Microsc. Res. Tech 2003;60:581–592. [PubMed: 12645006]
52. Heierhorst J, Mann RJ, Kemp BE. Interaction of the recombinant S100A1 protein with twitchin kinase, and comparison with other $Ca^{2+}$-binding proteins. Eur. J. Biochem 1997;24:127–133. [PubMed: 9363763]
53. Franz C, Durussel I, Cox JA, Schafer BW, Heizmann CW. Binding of $Ca^{2+}$ and $Zn^{2+}$ to human nuclear S100A2 and mutant proteins. J. Biol. Chem 1998;273:18826–18834. [PubMed: 9668057]
54. Fohr UG, Heizmann CW, Engelkamp D, Schafer BW, Cox JA. Purification and cation binding properties of the recombinant human S100 calcium-binding protein A3, an EF-hand motif protein with high affinity for zinc. J. Biol. Chem 1995;270:21056–21061. [PubMed: 7673133]
55. Schafer BW, Fritschy JM, Murmann P, Troxler H, Durussel I, Heizmann CW, Cox JA. Brain S100A5 is a novel calcium-, zinc-, and copper ion-binding protein of the EF-hand superfamily. J. Biol. Chem 2000;275:30623–30630. [PubMed: 10882717]
56. Kordowska J, Stafford WF, Wang CL. $Ca^{2+}$ and $Zn^{2+}$ bind to different sites and induce different conformational changes in human calcyclin. Eur. J. Biochem 1998;253:57–66. [PubMed: 9578461]
57. Pedrocchi M, Schafer BW, Durussel I, Cox JA, Heizmann CW. Purification and characterization of the recombinant human calcium-binding S100 proteins CAPL and CACY. Biochemistry 1994;33:6732–6738. [PubMed: 8204608]
58. Gribenko AV, Makhatadze GI. Oligomerization and divalent ion binding properties of the S100P protein: a $Ca^{2+}$/$Mg^{2+}$-switch model. J. Mol. Biol 1998;283:679–694. [PubMed: 9784376]
59. Korndorfer IP, Brueckner F, Skerra A. The crystal structure of the human (S100A8/S100A9)2 heterotetramer, calprotectin, illustrates how conformational changes of interacting alpha-helices can determine specific association of two EF-hand proteins. J. Mol. Biol 2007;370:887–898. [PubMed: 17553524]
60. Lee KC, Eckert RL. S100A7 (psoriasin)—mechanism of antibacterial action in wounds. J. Invest. Dermatol 2007;127:945–957. [PubMed: 17159909]
61. Glaser R, Harder J, Lange H, Bartels J, Christophers E, Schroder JM. Antimicrobial psoriasin (S100A7) protects human skin from *Escherichia coli* infection. Nat. Immunol 2005;6:57–64. [PubMed: 15568027]
62. Christianson DW. Structural biology of zinc. Adv. Protein Chem 1991;42:281–355. [PubMed: 1793007]
63. Vallee BL, Auld DS. Cocatalytic zinc motifs in enzyme catalysis. Proc. Natl Acad. Sci. USA 1993;90:2715–2718. [PubMed: 8464881]
64. Inman KG, Yang R, Rustandi RR, Miller KE, Baldisseri DM, Weber DJ. Solution NMR structure of S100B bound to the high-affinity target peptide TRTK-12. J. Mol. Biol 2002;324:1003–1014. [PubMed: 12470955]

65. Mori S, Abeygunawardana C, Johnson MO, van Zijl PC. Improved sensitivity of HSQC spectra of exchanging protons at short interscan delays using a new fast HSQC (FHSQC) detection scheme that avoids water saturation. J. Magn. Reson., Ser. B 1995;108:94–98. [PubMed: 7627436]
66. Mayer M, Meyer B. Group epitope mapping by saturation transfer difference NMR to identify segments of a ligand in direct contact with a protein receptor. J. Am. Chem. Soc 2001;123:6108–6117. [PubMed: 11414845]
67. Bax A, Davis DG. Practical aspects of two-dimensional transverse NOE spectroscopy. J. Magn. Reson 1985;63:207–213.
68. Delaglio F, Grzesiek S, Vuister GW, Zhu G, Pfeifer J, Bax A. NMRPipe: a multidimensional spectral processing system based on UNIX pipes. J. Biomol. NMR 1995;6:277–293. [PubMed: 8520220]
69. Edison AS, Abildgaard F, Westler WM, Mooberry ES, Markley JL. Practical introduction to theory and implementation of multi-nuclear, multidimensional nuclear magnetic resonance experiments. Methods Enzymol 1994;23:3–79. [PubMed: 7830587]
70. Live DH, Davis DG, Agosta WC, Cowburn D. Long range hydrogen bond mediated effects in peptides: $^{15}$N NMR study of gramicidin S in water and organic solvents. J. Am. Chem. Soc 1984;106:1939–1941.
71. Spera S, Bax A. Empirical correlation between protein backbone conformation and Ca and Cb/13-C nuclear magnetic resonance chemical shifts. J. Am. Chem. Soc 1991;113:5490–5492.
72. Otwinowski Z, Minor W. Processing of X-ray diffraction data collected in oscillation mode. Methods Enzymol 1997;276:307–326.
73. Vagin AA, Isupov MN. Spherically averaged phased translation function and its application to the search for molecules and fragments in electron-density maps. Acta Crystallogr., Sect. D: Biol. Crystallogr 2001;57:1451–1456. [PubMed: 11567159]
74. Murshudov GN, Vagin AA, Dodson EJ. Refinement of macromolecular structures by the maximum-likelihood method. Acta Crystallogr., Sect. D: Biol. Crystallogr 1997;53:240–255. [PubMed: 15299926]
75. Emsley P, Cowtan K. Coot: model-building tools for molecular graphics. Acta Crystallogr., Sect. D: Biol. Crystallogr 2004;60:2126–2132. [PubMed: 15572765]
76. Laskowski RA, MacArthur MW, Moss DS, Thornton JM. PROCHECK: a program to check the stereochemical quality of protein structures. J. Appl. Crystallogr 1993;26:283–291.
77. Laskowski RA, MacArthur MW, Thornton JM. Validation of protein models derived from experiment. Curr. Opin. Struct. Biol 1998;8:631–639. [PubMed: 9818269]
78. Yap KL, Ames JB, Swindells MB, Ikura M. Diversity of conformational states and changes within the EF-hand protein superfamily. Proteins: Struct. Funct. Genet 1999;37:499–507. [PubMed: 10591109]
79. Gagné SM, Tsuda S, Li MX, Smillie LB, Sykes BD. Structures of the troponin C regulatory domains in the apo and calcium-saturated states. Nat. Struct. Biol 1995;2:784–789. [PubMed: 7552750]
80. Berman HM, Westbrook J, Feng Z, Gilliland G, Bhat TN, Weissig H, et al. The Protein Data Bank. Nucleic Acids Res 2000;28:235–242. [PubMed: 10592235]
81. Yang H, Guranovic V, Dutta S, Feng Z, Berman HM, Westbrook JD. Automated and accurate deposition of structures solved by X-ray diffraction to the Protein Data Bank. Acta Crystallogr., Sect. D: Biol. Crystallogr 2004;60:1833–1839. [PubMed: 15388930]

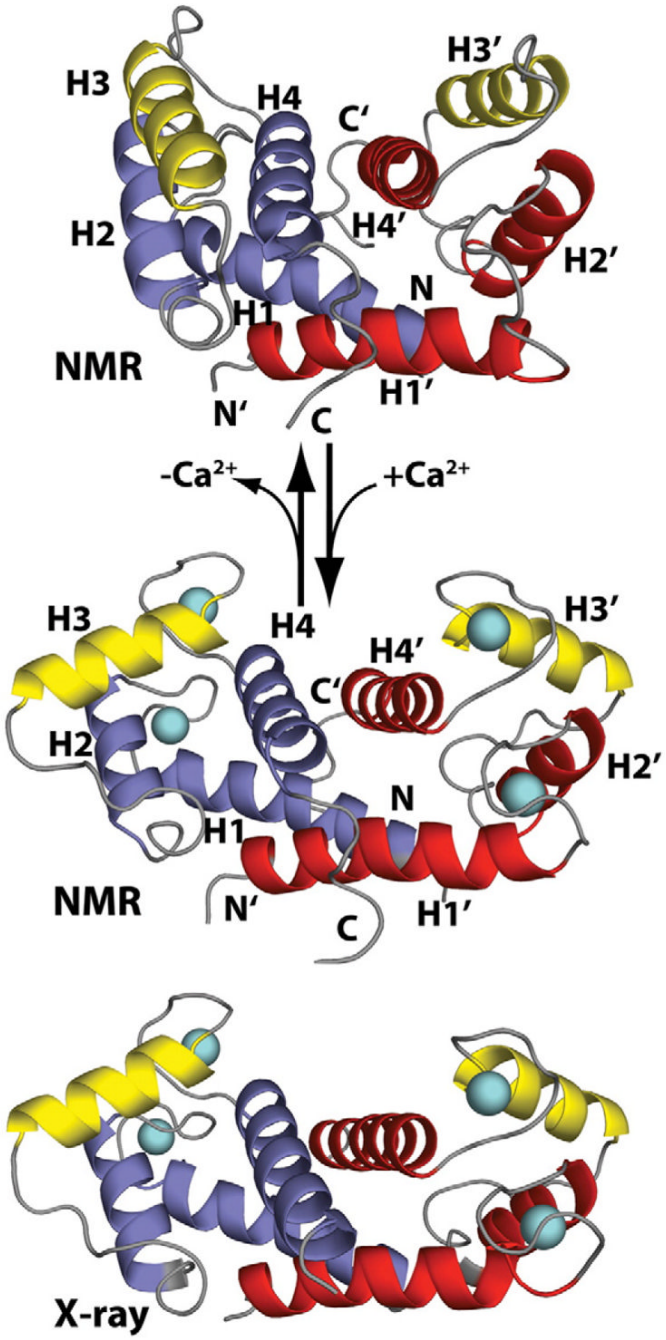


**Fig. 1.**

The "calcium switch" in S100B. Shown are ribbon diagrams of apo–S100B (NMR, PDB code: 1B4C) and $Ca^{2+}$-bound S100B (NMR, PDB code: 1QLK; X-ray, PDB code: 1MHO) illustrating the calcium-dependent reorientation of helix 3 (yellow) in each S100B subunit, termed the "$Ca^{2+}$ switch." The other three helices in each subunit of the symmetric S100B homodimer are colored red and blue, respectively. The loop regions of S100B are colored gray, and the two calcium ions per subunit are cyan spheres. This calcium-dependent conformational change is required for S100B to interact with specific protein targets such as p53.

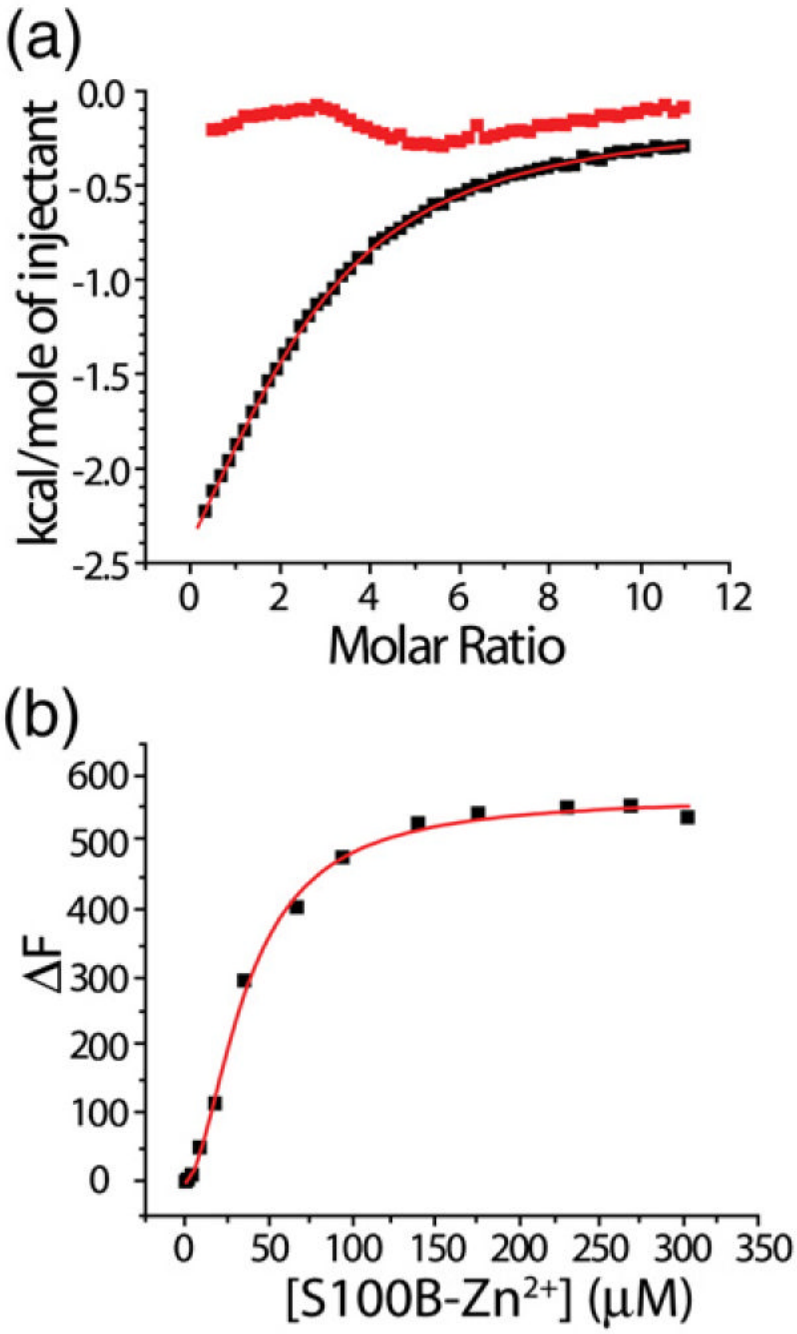


**Fig. 2.**

The binding of Pnt to $Ca^{2+}$–S100B and $Zn^{2+}$, $Ca^{2+}$–S100B. (a) Representative ITC data illustrating the binding of Pnt to $Ca^{2+}$–S100B (■; *n*=2). Conditions included 10 mM Tes, pH 7.2, 15 mM NaCl, and 10 mM $CaCl_2$, at 37 °C. Shown also is a control experiment illustrating no Pnt binding to S100B in the absence of calcium (red boxes). (b) Representative titration of $Zn^{2+}$–S100B (one $Zn^{2+}$ ion per S100B subunit) with $Ca^{2+}$ (10 mM) into a solution of Pnt and $Ca^{2+}$ (10 mM) as monitored by changes in Pnt fluorescence (*n*=1.7). Conditions included 10 mM Tes, pH 7.2, 15 mM NaCl, 100 mM KCl, and 10 mM $CaCl_2$, at 37 °C.

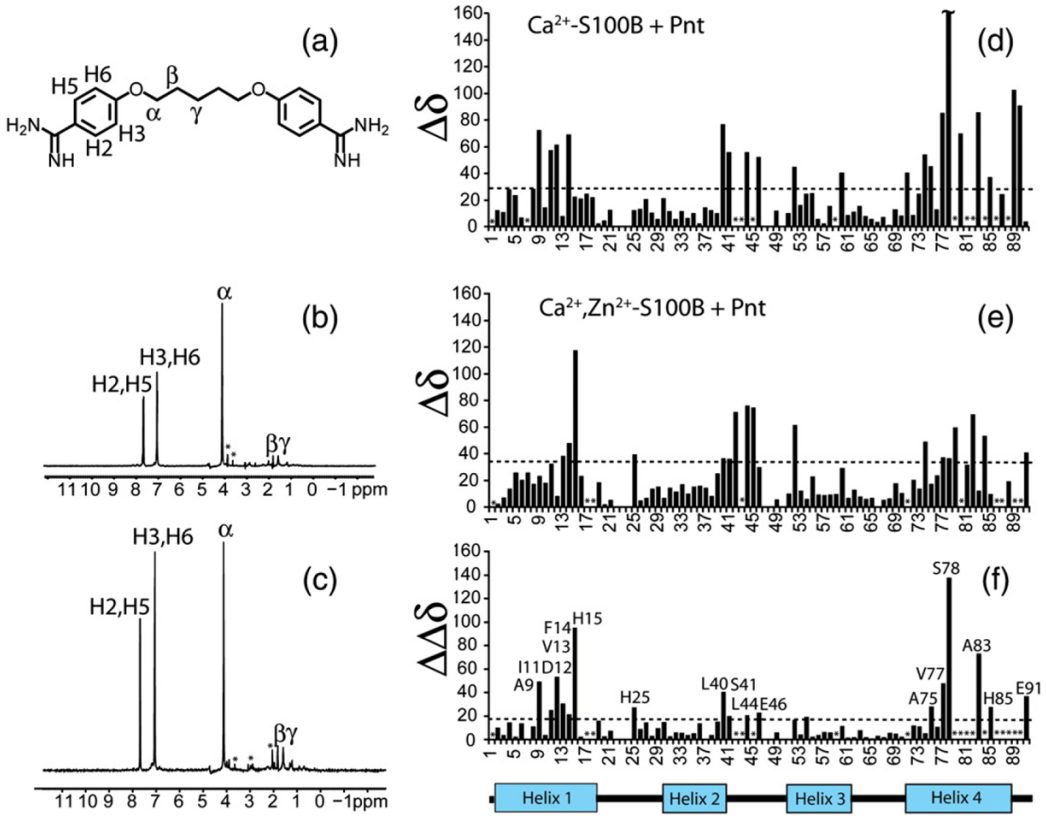


**Fig. 3.**

The binding of Pnt to $Ca^{2+}$–S100B and $Zn^{2+}$,$Ca^{2+}$–S100B as monitored by NMR spectroscopy. (a) Structure of Pnt together with the nomenclature used for protons of Pnt. (b and c) STD spectra for Pnt binding to (b) $Ca^{2+}$–S100B and to (c) $Zn^{2+}$,$Ca^{2+}$–S100B. (d and e) Perturbations in $^{1}H$ and $^{15}N$ chemical shift values for residues in S100B upon Pnt binding to (d) $Ca^{2+}$–S100B and to (e) $Zn^{2+}$,$Ca^{2+}$–S100B. (f) Differences in chemical shift perturbations when the titrations illustrated in (d) and (e) were compared (i.e., $|\Delta\delta^{Ca–S100B + Pnt} – \Delta\delta^{Zn,Ca–S100B + Pnt}|$).

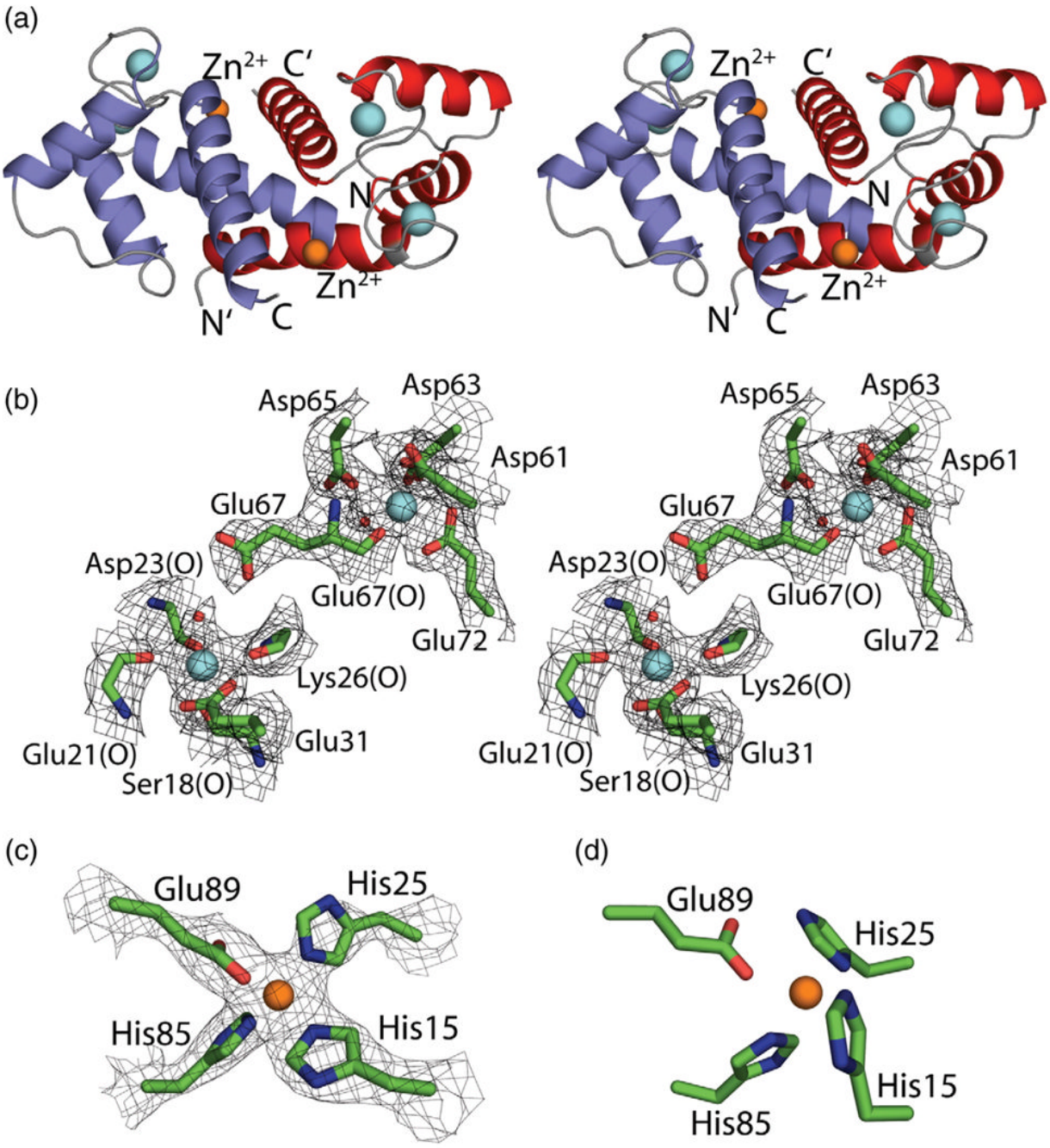


**Fig. 4.**

Calcium and zinc ion coordination in the X-ray structure of $Zn^{2+}$,$Ca^{2+}$–S100B. (a) X-ray crystal structure of $Zn^{2+}$,$Ca^{2+}$–S100B shown in stereo (walleye mode) as a ribbon diagram. The locations of two $Ca^{2+}$ ions per subunit (cyan spheres) and one $Zn^{2+}$ ion per subunit (orange spheres) are illustrated, and subunits of the symmetric S100B homodimer are colored red and blue, respectively. (b) Stereo view of the pseudo-EF-hand (Ser18, Glu21, Asp23, Lys26, and Glu31) and the canonical EF-hand (Asp61, Asp63, Asp65, Glu67, and Glu72) calcium-binding sites of S100B together with the $2mF_o–DF_c$ electron density map (1.0 σ). (c) $Zn^{2+}$ coordination in $Zn^{2+}$,$Ca^{2+}$–S100B is illustrated together with the $2mF_o–DF_c$ electron density map (1.0 σ) defining the positions of His15′/His25′ from one subunit of S100B and His85/Glu89 from the

other subunit. (d) Position of $Zn^{2+}$ coordinating residues of $Zn^{2+}$,$Ca^{2+}$–S100B as predicted previously from the NMR solution structure and site-directed mutagenesis.[7,8]

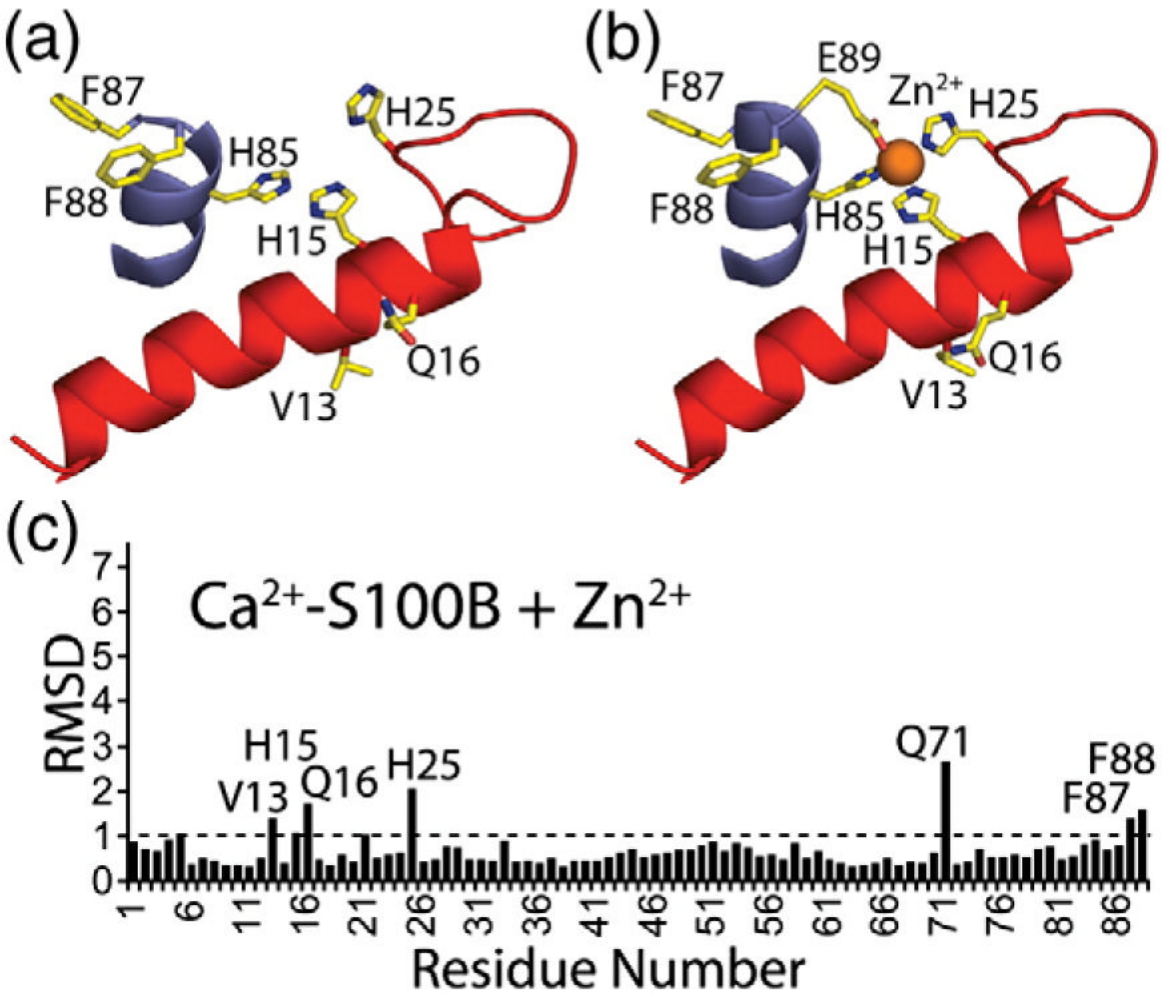


**Fig. 5.**

Changes in side-chain positioning upon the binding of $Zn^{2+}$ to $Ca^{2+}$–S100B. (a) Residues on helix 4 (blue) and helix 1′ (red) of $Ca^{2+}$–S100B prior to binding $Zn^{2+}$. (b) Residues on helix 4 (blue) and helix 1′ (red) of $Zn^{2+}$,$Ca^{2+}$–S100B that changed in position upon binding $Zn^{2+}$. (c) Average RMSDs for the position of side-chain atoms when the $Ca^{2+}$–S100B and $Zn^{2+}$,$Ca^{2+}$–S100B structures are compared. Those residues with average RMSD values greater than 1 are labeled on the bar graph.

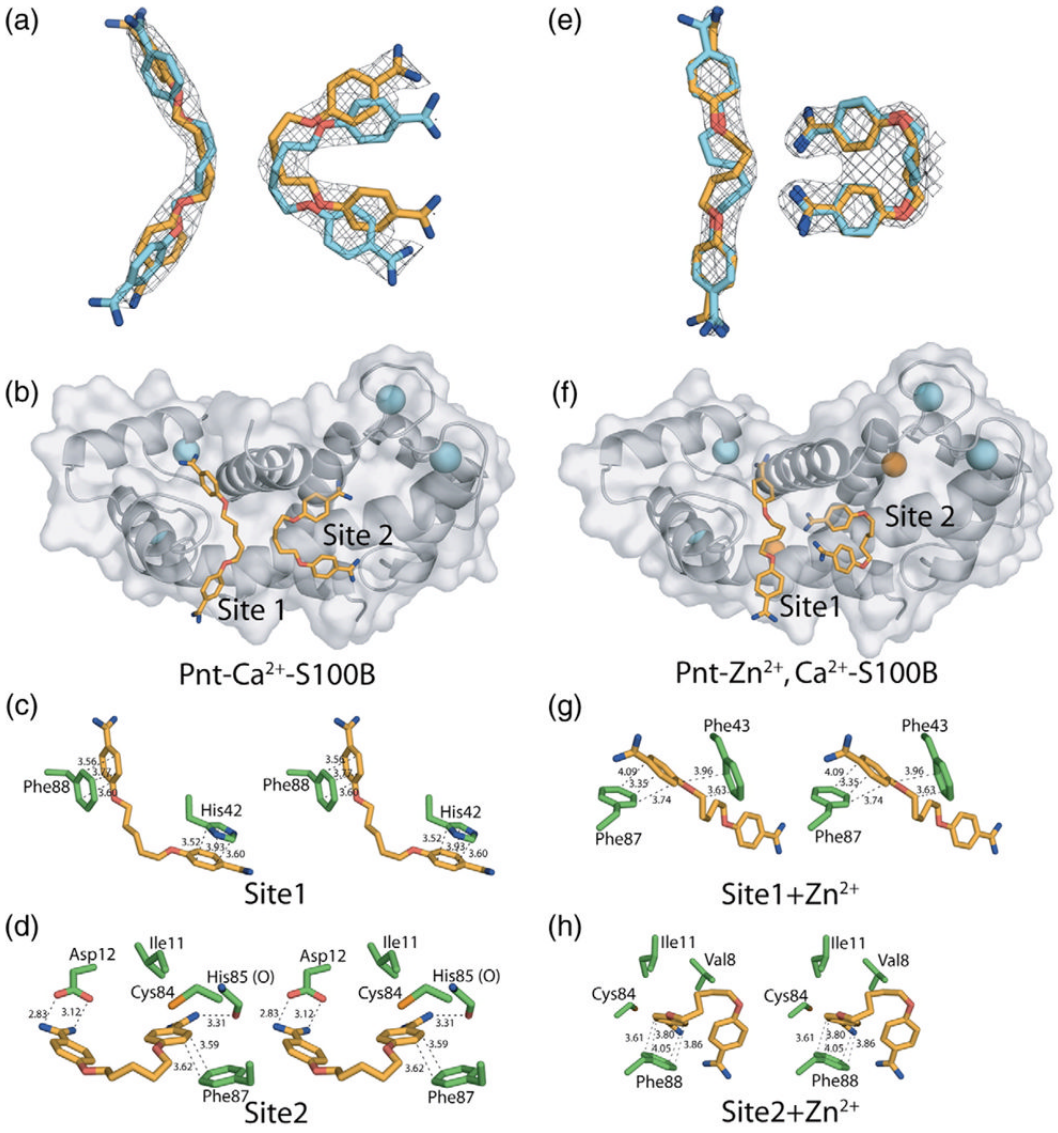


**Fig. 6.**

The X-ray structures of Pnt–$Ca^{2+}$–S100B and Pnt–$Zn^{2+}$,$Ca^{2+}$–S100B. (a) The $2mF_o$–$DF_c$ electron density maps (1.0 σ) for two Pnt molecules bound to $Ca^{2+}$–S100B (left: site 1, right: site 2). Symmetrical and overlapping orientations are shown for Pnt in each site (in orange and cyan) because of their locations at the crystallographic 2-fold axis. (b) Ribbon and surface diagram of Pnt–$Ca^{2+}$–S100B illustrating the location of Pnt (Pnt, orange; nitrogen, blue; oxygen, red) bound to sites 1 and 2 and $Ca^{2+}$ (cyan). (c) Residues of S100B that are within 4 Å of Pnt bound to site 1 in the Pnt–$Ca^{2+}$–S100B complex. (d) Residues of S100B that are within 4 Å of Pnt bound to site 2 in the Pnt–$Ca^{2+}$–S100B complex. (e) The $2mF_o$–$DF_c$ electron density maps (1.0 σ) for two Pnt molecules bound to $Zn^{2+}$,$Ca^{2+}$–S100B (left: site 1, right: site 2). Symmetrical and overlapping orientations are shown for Pnt in each site (in orange and cyan) because of their locations at the crystallographic 2-fold axis. (f) Ribbon and surface diagram of Pnt–$Zn^{2+}$,$Ca^{2+}$–S100B illustrating the location of Pnt (Pnt, orange; nitrogen, blue; oxygen, red) bound to sites 1 and 2, $Ca^{2+}$ (cyan), and $Zn^{2+}$ (orange). (g) Residues of S100B that are within 4 Å of Pnt bound to site 1 in the Pnt–$Zn^{2+}$,$Ca^{2+}$–S100B complex. (h) Residues of S100B that are within 4 Å of Pnt bound to site 2 in the Pnt–$Zn^{2+}$,$Ca^{2+}$–S100B complex.

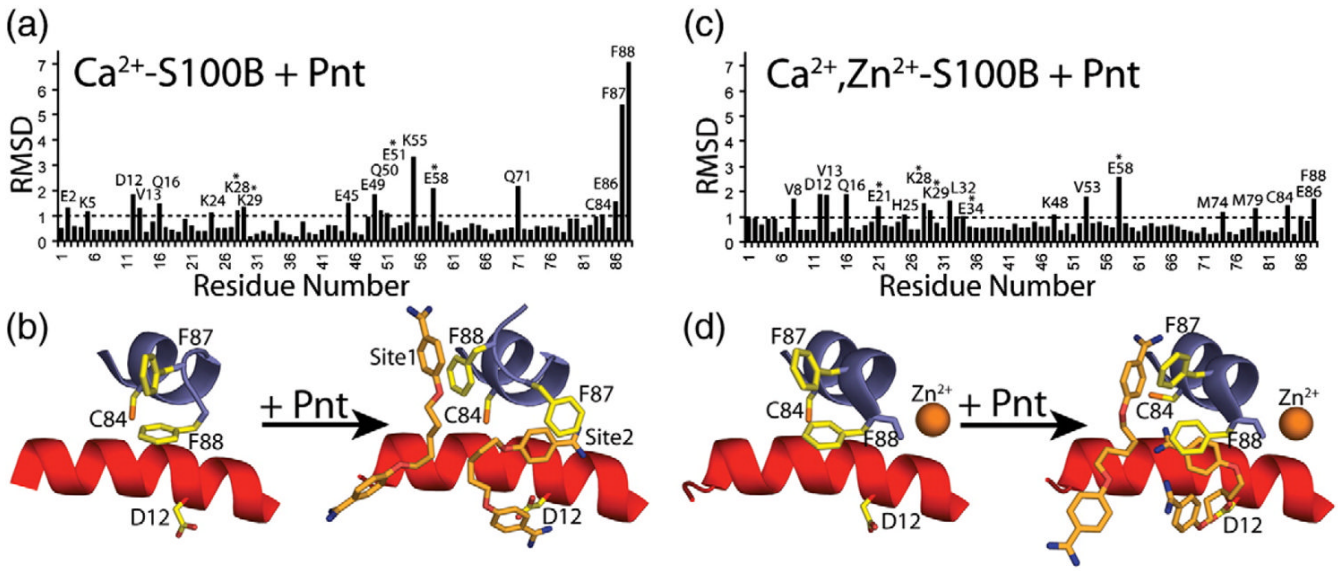


**Fig. 7.**

Changes in side-chain positioning upon the binding of Pnt to $Ca^{2+}$–S100B or to $Zn^{2+}$,$Ca^{2+}$–S100B. (a) Average RMSDs for the position of side-chain atoms when the X-ray structures of $Ca^{2+}$–S100B and Pnt–$Ca^{2+}$–S100B are compared. Those residues that have an average RMSD value greater than 1 are labeled, and residues marked with an asterisk (*) are involved with the crystallographic lattice. (b) Residues on helix 4 (blue) and helix 1′ (red) of $Ca^{2+}$–S100B in the absence and presence of Pnt (orange) illustrating the change in side-chain positioning upon drug binding. (c) Average RMSDs for the position of side-chain atoms when the X-ray structures of $Zn^{2+}$,$Ca^{2+}$–S100B and Pnt–$Zn^{2+}$,$Ca^{2+}$–S100B are compared. Those residues that have an average RMSD value greater than 1 are labeled, and residues marked with an asterisk (*) are involved with the crystallographic lattice. (d) Residues on helix 4 (blue) and helix 1′ (red) of $Zn^{2+}$,$Ca^{2+}$–S100B in the absence and presence of Pnt (orange) illustrating the change in side-chain positioning upon drug binding.

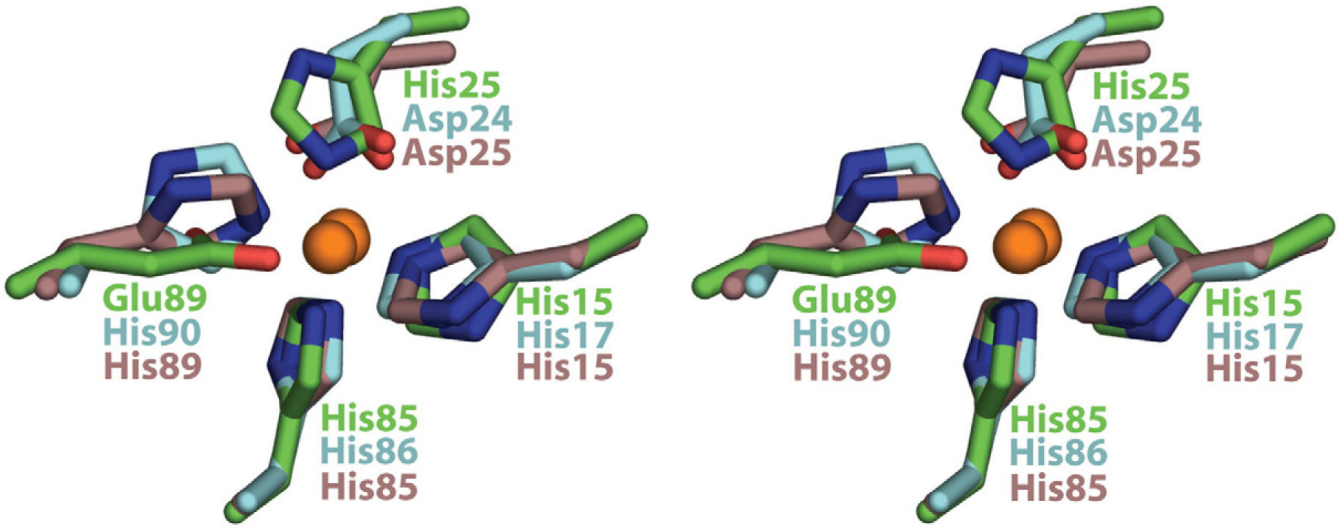


**Fig. 8.**

> A comparison of $Zn^{2+}$ or $Cu^{2+}$ coordination in S100B ($Zn^{2+}$), S100A7 ($Zn^{2+}$), and S100A12 ($Cu^{2+}$). Shown is an overlay of the $Zn^{2+}$/$Cu^{2+}$ligands for S100B (green, PDB code: 3CR2), S100A7[46] (cyan, PDB code: 2PSR), and S100A12[50] (violet, PDB code: 1ODB) as determined by X-ray crystallography.

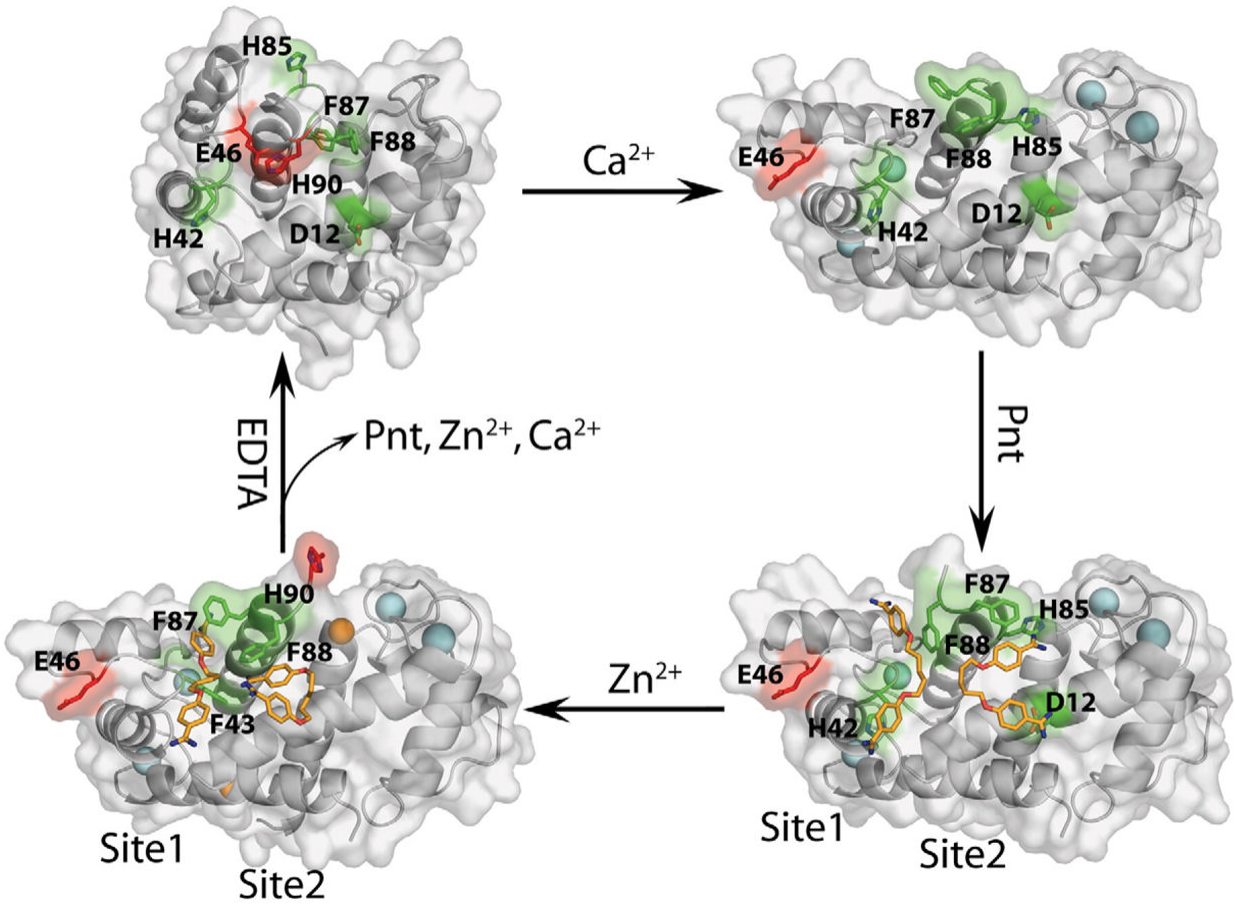


**Fig. 9.**

The calcium dependence of Pnt binding to S100B. Shown are ribbon/surface diagrams of apo–S100B (NMR, PDB code: 1B4C; top left), $Ca^{2+}$–S100B (X-ray, PDB code: 1MHO; top right), Pnt–$Ca^{2+}$–S100B (X-ray, PDB code: 3CR4; bottom right), and Pnt–$Zn^{2+}$,$Ca^{2+}$–S100B (X-ray, PDB code: 3CR5; bottom left). A hydrogen bond between His90 and Glu46 (red) that occludes both Pnt binding sites (residues in sites 1 and 2 are colored green) is observed in apo–S100B (top left). Upon binding $Ca^{2+}$ (top right), helix 3 reorients (see Fig. 1) and Glu46 is rotated out to the surface of the protein and His90 becomes dynamic and unobservable. Residues involved in Pnt binding two sites on S100B (highlighted in green) start to become localized as necessary for formation of the Pnt–$Ca^{2+}$–S100B complex (lower right). Upon binding $Zn^{2+}$,a second conformational change occurs, and surprisingly, Pnt is still able to bind both sites 1 and 2 (see also Figs. 6 and 7).

**Table 1**

Diffraction and refinement statistics

| | $Zn^{2+}$,$Ca^{2+}$-S100B | Pnt-$Ca^{2+}$-S100B | Pnt-$Zn^{2+}$,$Ca^{2+}$-S100B |
|---|---|---|---|
| *Diffraction statistics* | | | |
| Space group | $C222_1$ | $P4_12_12$ | $P4_12_12$ |
| Cell dimensions: *a*, *b*, *c* (Å) | 34.6, 90.5, 58.3 | 63.6, 63.6, 48.2 | 62.9, 62.9, 50.1 |
| Cell angles: α, β, γ (°) | 90, 90, 90 | 90, 90, 90 | 90, 90, 90 |
| Resolution (Å) | 45.22–1.88 (1.93–1.88) | 44.95–2.15 (2.20–2.15) | 44.46–1.85 (1.90–1.85) |
| No. of unique reflections | 7120 (502) | 5502 (390) | 8456 (560) |
| Completeness (%) | 96.45 (91.90) | 99.98 (99.76) | 98.84 (93.20) |
| $R_{sym}$ [a] | 0.056 (0.319) | 0.081 (0.667) | 0.150 (0.489) |
| Average $I/\sigma$ | 23.4 (4.3) | 32.3 (4.2) | 20.4 (4.2) |
| Multiplicity | 6.6 (5.1) | 12 (12.1) | 12.9 (8.9) |
| *Refinement statistics* | | | |
| $R_{crys}$ [b](%) | 22.1 (31.1) | 21.1 (25.2) | 19.4 (21.2) |
| $R_{free}$ [b](%) | 26.8 (46.7) | 26.6 (26.7) | 24.3 (22.9) |
| Protein atoms | 727 | 729 | 737 |
| Water molecules | 51 | 35 | 82 |
| Non-hydrogen atoms | 768 | 814 | 858 |
| Mean *B* values (Å$^2$) | | | |
| Overall | 49.42 | 35.87 | 40.16 |
| Protein atoms | 50.19 | 35.05 | 39.01 |
| Water molecules | 51.34 | 35.59 | 45.94 |
| $Ca^{2+}$ typical EF hand | 47.00 | 31.72 | 35.76 |
| $Ca^{2+}$ S100B EF hand | 46.71 | 35.58 | 35.63 |
| $Zn^{2+}$ | 50.11 | | 43.17 |
| Pnt site 1 | | 53.14 [c] | 49.85 [d] |
| Pnt site 2 | | 43.01 [c] | 67.52 [d] |
| RMSD | | | |
| Bond length (Å) | 0.015 | 0.008 | 0.015 |
| Bond angles (Å) | 1.543 | 1.135 | 1.484 |
| Ramachandran plot (%) [e] | | | |
| Most favored | 95.2 | 95.2 | 96.5 |
| Additionally allowed | 4.8 | 4.8 | 3.5 |
| PDB identification | 3CR2 | 3CR4 | 3CR5 |

Numbers in parentheses represent the last outer shell.

[a] $R_{sym} = \Sigma_{hkl}\Sigma_i(|I_{hkl,i}|-|\langle I_{hkl}\rangle|)/\Sigma_{hkl}\Sigma_i I_{hkl,i}$, for a reflection *hkl* whose weighted mean over *i* observations is $\langle I\rangle$s.

[b] $R_{Crys}$ and $R_{free} = \Sigma_{hkl}||F_O|-k|F_C||/\Sigma_{hkl}||F_O|$, where $|F_O|$ is the observed structure factor amplitude and $|F_C|$ is the calculated structure factor amplitude for the working and test sets, respectively.

[c] Mean *B* values (Å$^2$) for Pnt in sites 1 and 2 are similar to the mean *B* value (38.74) for side-chain atoms of S100B involved in Pnt binding (Ile11, Asp12, His42, Cys84, Phe87, and Phe88).

[d] Mean *B* values (Å$^2$) for Pnt in sites 1 and 2 are similar to the mean *B* value (45.29) for side-chain atoms of S100B involved in the Pnt binding (Val8, Ile11, Phe43, Cys84, Phe87, and Phe88).

[e] For $Zn^{2+}$,$Ca^{2+}$-S100B and Pnt-$Ca^{2+}$-S100B, the calculations had 80 residues in the most favored region and 4 residues in additionally allowed regions. For Pnt-$Zn^{2+}$,$Ca^{2+}$-S100B, the calculations had 82 residues in the most favored region and 3 residues in additionally allowed regions.

**Table 2**

Dissociation constants ($K_d$) and enthalpy ($\Delta H_{app}$) and entropy ($T\Delta S$) for Pnt and $Zn^{2+}$ binding to S100B

| | $K_d$ (μM), ITC | $\Delta H_{app}$ (kcal/mol) | $T\Delta S$ (kcal/mol) | $K_d$ (μM), fluorescence |
|---|---|---|---|---|
| *Pnt* | | | | |
| $Ca^{2+}$-S100B (low salt)[a,b] | 53±10[c] | −4.0±0.2 | 2.1±0.2[d] | 39±3 |
| $Ca^{2+}$-S100B (high salt)[a,b] | 50±5[c] | −4.6±0.4 | 1.5±0.4[d] | 44±4 |
| $Zn^{2+}$,$Ca^{2+}$-S100B (low salt)[e,f] | 64±15 | −5.0±0.1 | 1.0±0.2[d] | 39±5 |
| $Zn^{2+}$,$Ca^{2+}$-S100B (high salt)[b,e] | 35±12[c] | −4.3±0.5 | 1.6±0.5[d] | 40±5 |
| *$Zn^{2+}$* | | | | |
| Pnt-$Ca^{2+}$-S100B (low salt)[g] | 0.13±0.09 | −7.6±0.5 | 2.1±0.4[d] | - |
| $Ca^{2+}$-S100B (low salt)[h] | 0.09±0.02[h] | −6.2±0.1[h] | 3.8±0.1[d,h] | - |

[a] Conditions included 10 mM TES, pH 7.2, 15 mM NaCl, and 10 mM $CaCl_2$, at 37 °C. For the high-salt conditions, 100 mM KCl.

[b] A single dissociation constant ($K_d$) is reported even though two sites for Pnt binding were detected by ITC for these complexes ($n$ = 1.9±0.2). As expected, the fluorescence data also are best fit with a two-site model ($n_{measured}$ = 1.8±0.2) for both the Pnt-$Ca^{2+}$-S100B and Pnt-$Zn^{2+}$,$Ca^{2+}$-S100B complex. That $n_{measured}$ used to fit the fluorescence data is less than or equal to $n$ as determined from ITC is also consistent with having two noninteracting Pnt sites. Thus, the simplest model that fits the data under these conditions is that two independent Pnt binding sites exist with indistinguishable affinities.

[c] The $c$ values range from 3 to 5 for the ITC experiments, indicating that the binding data are appropriate for evaluating $K_d$ values.

[d] An estimate for the entropic contribution to binding ($T\Delta S$) was calculated using the dissociation constant ($K_d$) and the apparent molar enthalpy of association ($\Delta H_{app}$) for Pnt binding.

[e] Conditions included 10 mM TES, pH 7.2,15 mM NaCl, 10 mM $CaCl_2$, and 100–500 μM $ZnCl_2$, at 37 °C. For the high-salt conditions, 100 mM KCl was added. For the fluorescence titrations in the presence of $Zn^{2+}$, the $Zn^{2+}$-to-S100B ratio did not exceed 1:1 to avoid precipitation (see Materials and Methods).

[f] The ITC data for $Zn^{2+}$,$Ca^{2+}$-S100B under low-salt conditions was evaluated ($K_d$~64±15), but due to large amounts of precipitation at high Pnt levels, the stoichiometry was not reliably determined, and this dissociation constant is only considered an estimate. At lower protein concentrations, the fluorescence data were more reliable ($K_d$ = 39±5; $n_{measured}$ = 1.8±0.1).

[g] Conditions included 10 mM TES, pH 7.2,15 mM NaCl, 10 mM $CaCl_2$, and 100–400 μM Pnt, at 37 °C with $c$ values ranging from 700 to 1000.

[h] Conditions included 10 mM TES, pH 7.2, 15 mM NaCl, and 10 mM $CaCl_2$, at 37 °C, and the value is from Wilder *et al.*[8]

**Table 3**

Divalent metal ion and water coordinate distances

| | $Ca^{2+}$-S100B[a] | $Zn^{2+}$,$Ca^{2+}$-S100B | Pnt-$Ca^{2+}$-S100B | Pnt-$Zn^{2+}$,$Ca^{2+}$-S100B |
|---|---|---|---|---|
| *$Zn^{2+}$* | | | | |
| His15 ($N^{\varepsilon 2}$) | | 2.0 | | 2.0 |
| His25 ($N^{\varepsilon 2}$) | | 1.9 | | 2.2 |
| His85 ($N^{\varepsilon 2}$) | | 2.0 | | 2.0 |
| Glu89 ($O^{\varepsilon 1}$ or $O^{\varepsilon 2}$) | | 2.0 | | 1.9 |
| *$Ca^{2+}$, pseudo-EF hand* | | | | |
| Ser18 (C=O) | 2.0 | 2.3 | 2.3 | 2.3 |
| Glu21 (C=O) | 2.3 | 2.6 | 2.3 | 2.3 |
| Asp23 (C=O) | 2.6 | 2.5 | 2.3 | 2.3 |
| Lys26 (C=O) | 2.3 | 2.3 | 2.4 | 2.3 |
| Glu31 ($O^{\varepsilon 1}$,$O^{\varepsilon 2}$) | 2.4, 2.6 | 2.3, 2.5 | 2.5, 2.6 | 2.5, 2.6 |
| $H_2O$[b] | 2.2 | 2.5 | 2.5 | 2.3 |
| *$Ca^{2+}$, canonical EF hand* | | | | |
| Asp61 ($O^{\Delta 1}$ or $O^{\delta 2}$) | 2.3 | 2.3 | 2.3 | 2.4 |
| Asp63 ($O^{\delta 1}$ or $O^{\delta 2}$) | 2.6 | 2.4 | 2.4 | 2.5 |
| Asp65 ($O^{\delta 1}$ or $O^{\delta 2}$) | 2.3 | 2.6 | 2.4 | 2.4 |
| Glu67 (C=O) | 2.4 | 2.4 | 2.4 | 2.4 |
| Glu72 ($O^{\varepsilon 1}$,$O^{\varepsilon 2}$) | 2.3, 2.5 | 2.4, 2.7 | 2.5, 2.6 | 2.3, 2.5 |
| $H_2O$[c] | 2.4 | 2.3 | 2.3 | 2.4 |
| *$Ca^{2+}$-bound $H_2O$* | | | | |
| Asp65 ($O^{\delta 1}$ or $O^{\delta 2}$)[c] | 2.8 | 2.4 | 2.7 | 2.6 |
| Glu67 ($O^{\varepsilon 1}$ or $O^{\varepsilon 2}$)[b] | 2.6 | 2.9 | 2.8 | 2.7 |

All distances are in angstroms and are from nitrogen, oxygen, or $Ca^{2+}$. Distances between the two $Ca^{2+}$ ions for the $Ca^{2+}$-S100B, $Zn^{2+}$,$Ca^{2+}$-S100B, Pnt-$Ca^{2+}$-S100B, and Pnt-$Zn^{2+}$,$Ca^{2+}$-S100B structures are 11.5, 11.5, 11.4, and 11.4 Å, respectively.

[a] Calculated using PDB entry 1MHO.

[b] $H_2O$ ligands to $Ca^{2+}$ from the pseudo-EF hand.

[c] $H_2O$ ligands to $Ca^{2+}$ from the canonical EF hand.

**Table 4**

Interhelical angles and distances

| | Interhelical angle (°) | | | | | | | | Interhelical distance (Å) | |
|---|---|---|---|---|---|---|---|---|---|---|
| | I to II | I to III | I to IV | II to III | II to IV | III to IV | I to I′ | IV to IV′ | I to I′ | IV to IV′ |
| $Ca^{2+}$-S100B[a,b] | 140 | −121 | 125 | 99 | −32 | 110 | −152 | 150 | 13.7 | 10.0 |
| $Zn^{2+}$,$Ca^{2+}$-S100B[a] | 142 | −120 | 126 | 97 | −32 | 110 | −151 | 148 | 13.7 | 10.2 |
| Pnt-$Ca^{2+}$-S100B[a] | 139 | −121 | 125 | 99 | −32 | 109 | −152 | 146 | 13.6 | 10.1 |
| Pnt-$Zn^{2+}$,$Ca^{2+}$-S100B[a] | 139 | −122 | 125 | 98 | −32 | 109 | −151 | 146 | 13.6 | 10.0 |

Interhelical angles were calculated using INTERHLX software (K. Yap, University of Toronto) except for I to I′ and IV to IV′ where the interhelical angles and distances were determined using IHA v1.4 (S.M. Gagne, SMG Software Inc.).

[a] The residues defining each helix of S100B were as follows: helix I, residues 2–18; helix II, residues 29–40; helix III, residues 50–62; and helix IV, residues 70–82.

[b] Calculated using PDB entry 1MHO.

**Table 5**

EF-hand angles determined using the vector geometry mapping (VGM) method

| | N-terminal coordinate of second helix | | | Θ (°) | Φ (°) | Ω (°) |
|---|---|---|---|---|---|---|
| *Pseudo-EF hand* | | | | | | |
| $Ca^{2+}$-S100B[a,b] | 8.2 | −0.2 | −6.8 | 50 | 87 | 109 |
| $Zn^{2+}$,$Ca^{2+}$-S100B[a] | 8.2 | 0.0 | −6.4 | 50 | 87 | 108 |
| Pnt-$Ca^{2+}$-S100B[a] | 8.3 | −0.1 | −6.5 | 51 | 91 | 107 |
| Pnt-$Zn^{2+}$,$Ca^{2+}$-S100B[a] | 8.2 | 0.0 | −6.7 | 51 | 90 | 105 |
| *Typical EF hand* | | | | | | |
| $Ca^{2+}$-S100B[a,b] | 8.9 | 0.3 | −6.6 | 74 | 102 | 75 |
| $Zn^{2+}$,$Ca^{2+}$-S100B[a] | 8.8 | −0.2 | −6.8 | 76 | 104 | 75 |
| Pnt-$Ca^{2+}$-S100B[a] | 8.8 | 0.4 | −6.5 | 74 | 104 | 69 |
| Pnt-$Zn^{2+}$,$Ca^{2+}$-S100B[a] | 8.8 | 0.3 | −6.5 | 75 | 105 | 70 |

VGM angles were calculated by way of VGM software (K. Yap, University of Toronto) using the helices and structures indicated.

[a] The residues used for the VGM calculations were as follows: helix I, residues 10–17; helix II, residues 29–39; helix III, residues 53–60; and helix IV, residues 70–80.

[b] Calculated using PDB entry 1MHO.